Spectral Observations of Diffuse FUV Emission from the Hot Phase of the Interstellar Medium with DUVE (the Diffuse Ultraviolet Experiment)

by

Eric John Korpela

B.S. (University of Wisconsin) 1988

A dissertation submitted in partial satisfaction

of the requirements for the degree of

Doctor of Philosophy

in

Astronomy

in the

GRADUATE DIVISION

of the

UNIVERSITY OF CALIFORNIA, BERKELEY

Spring, 1997

Committee in charge:

Professor C. Stuart Bowyer, Chair
Professor Carl Heiles
Professor Robert Lin
Professor William J. Welch

The dissertation of Eric John Korpela is approved:

Professor C. Stuart Bowyer, Chair	Date
Professor Carl Heiles	Date
Professor Robert Lin	Date
Professor William J. Welch	Date

University of California, Berkeley

Spring, 1997

Spectral Observations of Diffuse FUV Emission from the Hot Phase of the Interstellar Medium with DUVE (the Diffuse Ultraviolet Experiment)

by

Eric John Korpela

Abstract

One of the keys to understanding the structure and distribution of interstellar matter in the galaxy is understanding the distribution of the low density hot (10^5 K $- 10^6$ K) phase of the interstellar medium (ISM). Because of its low density and lack of easily observable tracers, this phase is much more difficult to observe than the cooler high density components of the ISM. Because gas of this temperature emits mainly in the far ultraviolet (912 Å - 1800 Å), extreme ultraviolet (80 Å - 912 Å), and (for gas hotter than 10^6 K) X-rays, observations in these bands can provide important constraints to the distribution of this gas. Because of interstellar opacity at EUV wavelengths, only FUV and X-ray observations can provide clues to the properties of hot gas outside the immediate solar neighborhood. I present results from a search for FUV emission from the diffuse ISM conducted with an orbital FUV spectrometer, DUVE, which was launched in July, 1992. The DUVE spectrometer, which covers the band from 950 Å to 1080 Å with 3.2 Å resolution, observed a region of low neutral hydrogen column density near the south galactic pole for a total effective integration time of 1583 seconds. The only emission line detected was a geocoronal hydrogen line at 1026 Å . I am able to place upper limits to several emission features that provide constraints to interstellar plasma parameters. I am also able to place limits to continuum emission throughout the bandpass. I compare these limits and other diffuse observations with several models of the structure of the interstellar medium and discuss the ramifications of these models.

Chairman _____


USAF
MOSSC
JCWS
DELTA
GEOTAIL
NASA

Science is a wonderful thing if one does not have to earn a living at it.

Albert Einstein

Contents

List of Figures

List of Tables

Acknowledgements

It would double the length of this thesis to list the individual contributions of everyone who helped get DUVE off the ground and the results on paper. Without advice, support and an occasional kick in the pants from Professor Stuart Bowyer, the DUVE instrument would have remained firmly on the ground.

I'd like to thank Jerry Edelstein for originally hiring me to help with his thesis project and designing the instrument that was modified for this work. Without the assistance of Ray Chung, Josef Dalcolmo, Don Zukauckas, Chris Scholz, Jerry Penegor, Mike Sholl, Chrissy Underwood, Akos Szbozlay, Trey Roessig, and Larry Wong the instrument could not have been built. Without the assistance of Charlie Gunn at NASA headquarters, DUVE never would have gotten off the ground.

I'd like to thank the crews at McDonnell-Douglas, NASA/OLS, and KSC/CCAFS especially Darren Bedell, Mike Hallett, Larry Berge, Tom Alexiou, Beth Cerrato, Diane Silva and Skip Mackey for treating us like important customers and showing us where to to get the best rock shrimp. I wish the rest of the aerospace industry had their level of professionalism.

My parents deserve a lot of credit for encouraging my interest in astronomy by buying me that telescope 20 years ago. They also encouraged me to stick with it, even when the money was calling me elsewhere.

I wouldn't have gotten through these years of work without the support of friends like Shauna Sallmen, Steve Fulton, Areiel Wolanow, Sonia Connolly, and Angela Haskell.

And of course, all of my love and thanks to my wife, Angela, for believing in me even when I didn't.

This work has been supported by NASA grant NGR-05-003-805.

Chapter 1

A Brief History of the Hot Interstellar Medium

In 1956, Lyman Spitzer noted that small, cool clouds of neutral hydrogen existed hundreds of parsecs above the galactic plane [49]. Because these clouds were far too small to be gravitationally bound, they would have dissipated over extremely short timescales. For these clouds to exist at all, they would have to be confined by an external pressure. With this in mind, Spitzer postulated the existence of a corona of hot gas that supplies this pressure. He reasoned that gas at about 10^6 K could provide the required pressure at a very low density. Gas at this temperature and density would have no observable optical emission. Because there was no way of testing this prediction at the time, it was promptly forgotten.

1.1 The soft X-ray background

Ten years later, Bowyer, Field, and Mack launched a sounding rocket to investigate the diffuse soft X-ray background [5]. Their rocket contained two thin window proportional counters for the C band (.160-.284 keV).

The results of these observations were notable in several respects. The observations indicated significantly more emission than would be expected from an extrapolation of observations at higher energies (1-100 keV). This indicated that it was

likely that a different mechanism was responsible for the soft X-ray emission.

They initially assumed that the source of this soft X-ray excess was extragalactic, like the higher energy X-rays. However, the effective absorption they calculated was $\frac{1}{3}$ of the expected theoretical value. They explained this weakened absorption as evidence of clumping of the absorbing HI along the line of sight.

The intensity of the emission they observed was highly variable with respect to the direction observed. This was to be expected as the interstellar medium is far more opaque near $\frac{1}{4}$ keV than it is at higher energies. However, the ratio of the intensity at the galactic pole and that near the galactic plane was only about two. Given the cross section of hydrogen at $\frac{1}{4}$ keV (7.9×10^{-21} cm^{-2}) and a typical interstellar density near the galactic plane (1 cm^{-3}), we can quickly calculate a photon mean free path of 40 pc . Unlike the emission seen at higher energies, a significant fraction of this emission had to be coming from the solar neighborhood.

Other experiments, most recently ROSAT, have mapped this soft X-ray emission with high spatial resolution [48]. Cloud shadowing studies show that about 65% of the $\frac{1}{4}$ keV emission at high galactic latitude arises in the local interstellar medium. About 7% seems to arise in the galactic halo and about 28% seems to arise outside of the galaxy. These ratios are highly variable on small angular scales [33].

1.2 The Smith and Cox model

For many years following the discovery of hot interstellar gas, the question of its origin went unanswered in detail. In 1974, Smith and Cox published an estimate of the volume of space that could be filled by hot gas from supernova remnants [46]. Their estimate assumed supernovae randomly distributed with an exponential scale height in a medium with uniform density. The resulting estimate was that 10-15% of the volume at the galactic plane could be filled by these remnants. It should be noted that this simple estimate has several weaknesses. It assumes that supernovae occur randomly throughout space, when they are far more likely to occur in clusters. The estimate is also highly dependent on the density and uniformity of the ambient medium.

Smith and Cox also noted that there was no existing observational constraint on the filling factor of these remnants. They conjectured that given sufficient filling factor, adjacent remnants could interact forming tunnels through the neutral medium. Their model, however, was unable to explain how gas from these remnants could reach the galactic halo to produce the soft X-ray emission seen at high galactic latitude.

1.3 OVI absorption lines

In that same year, the Copernicus satellite, an FUV spectrometer, detected the presence of absorption lines due to OVI $\lambda\lambda$ 1032,1038 in the spectra of several O and B stars. For OVI to have sufficient abundance to cause this absorption, significant quantities of plasma at a temperature near $10^{5.3}$ would need to be present in the interstellar medium. I will discuss the characteristics and significance of these absorption lines in Chapter 2.

1.4 The galactic fountain

In 1976, Shapiro and Field theorized that hot gas from supernovae could get to high galactic scale height through a "galactic fountain" process [38]. In this model hot, overpressured gas in supernovae remnants rises buoyantly from the galactic plane to scale heights approaching 1 kpc . Once there, the gas cools radiatively, condenses into clouds due to instabilities, and these clouds fall back toward the disk. This model can explain both the presence of hot gas at high scale heights and the presence of infalling neutral clouds at a range of velocities. These infalling clouds had been seen in 21 cm HI emission [52, 53]. The question of whether correlated supernovae can produce superbubbles which can break through the combined gas and magnetic pressure of the galactic disks is still the subject of much debate [9].

1.5 The McKee-Ostriker model

The following year, McKee and Ostriker described a model of the interstellar medium which differed from earlier models in that the dominant phase of the ISM was a hot, low-density phase filling 60% of the volume of the ISM [29]. In their model the hot phase, at a temperature of about $10^{5.5}$ K to $10^{6.3}$ K and density of 10^{-2} cm^{-3}, exists in pressure equilibrium with clouds of warm (T$\sim 10^4$ K) and cold (T$\sim 10^2$ K) gas filling the remainder of space. This hot gas is generated in supernova explosions, and is well distributed throughout space due to the low density of the ambient medium. It is cooled by a combination of emission of soft X-ray and ultraviolet radiation from high stage ions and through conductive evaporation at the surface of the neutral clouds. They proposed that these conductive interfaces could explain the line profiles and ionization levels of oxygen seen by the Copernicus satellite.

In addition, this model can be used to explain the nearby portion of the soft X-ray background as arising directly in the dominant hot gas. If this is the case, the model predicts that the outer layers of these clouds would be photoionized by the X-rays. A sky background of Hα emission from gas which could result from such photoionized layers has been seen, and has been investigated in detail by Reynolds [32].

1.6 Recent developments

Since 1980, many absorption lines from high stage ions (CIV , SiIV , NV) have been observed as arising in the interstellar medium of the galactic disk and halo [35, 37]. (The properties of these lines will be discussed in the next chapter.) Because of the difficulty of diffuse emission line studies, very few FUV and EUV lines produced in hot interstellar gas have been detected in emission. One notable exception is the detection of emission due to CIV $\lambda\lambda$ 1548,1551 seen at high galactic latitude by Martin and Bowyer [27]. The interpretation has been that these lines indicate the presence of gas at a temperature of 10^5 K in the galactic halo with scale heights of up to a few kiloparsecs.

On the theoretical front, some have begun to question the idea that the hot interstellar medium fills a large fraction of the interstellar volume. The roles of magnetic field in confining supernova remnants has been explored by Cox and collaborators, who have concluded that the filling fraction of the hot interstellar medium in the galactic plane due to these remnants is less than 20% [44, 45, 40, 9]. In addition, the constraints of hydrostatic equilibrium require that pressures in the galactic plane be $\sim$ 25,000 cm^{-3}K , potentially causing further confinement of hot gas.

In addition, alternative theories to explain the presence of high stage ions in the galactic halo and the heating mechanisms for hot gas have been put forward, most notably cosmic ray supported halos [7] and microflaring [31]. These theories are notable in that they do no require a large filling factor of hot gas at low z in order to heat the galactic halo. These theories, however, have yet to gain a substantial following.

Chapter 2

Past FUV observations of the interstellar medium

As is shown in Figure 2.1, the main contributions to the equilibrium radiative cooling curve near its peak between $10^{5.5}$ K and 10^{7} K are from lines in the FUV and EUV region of the spectrum [26]. Thus we would expect these lines to be brightest in radiatively cooling gas at these temperatures. While nonequilibrium ionization may be more appropriate, the details are contested among workers in the field. Because of the complexities involved, virtually all experimental results are interpreted in terms of collisional ionization equilibrium. Even in the case of nonequlibrium ionization, FUV and EUV emission lines are important cooling mechanisms for hot gas. Because the interstellar medium is very opaque to EUV radiation, observations in that band are restricted to the local interstellar medium. To determine conditions on galactic scales, FUV observations must be made.

2.1 FUV absorption measurements

In the past several decades, measurements of FUV absorption of many highly ionized species have been made using Copernicus, IUE and more recently the Goddard High Resolution Spectrometer (GHRS) on the Hubble Space Telescope, and the Berkeley FUV/EUV Spectrometer on ORFEUS. [35, 37, 50]. These observations of

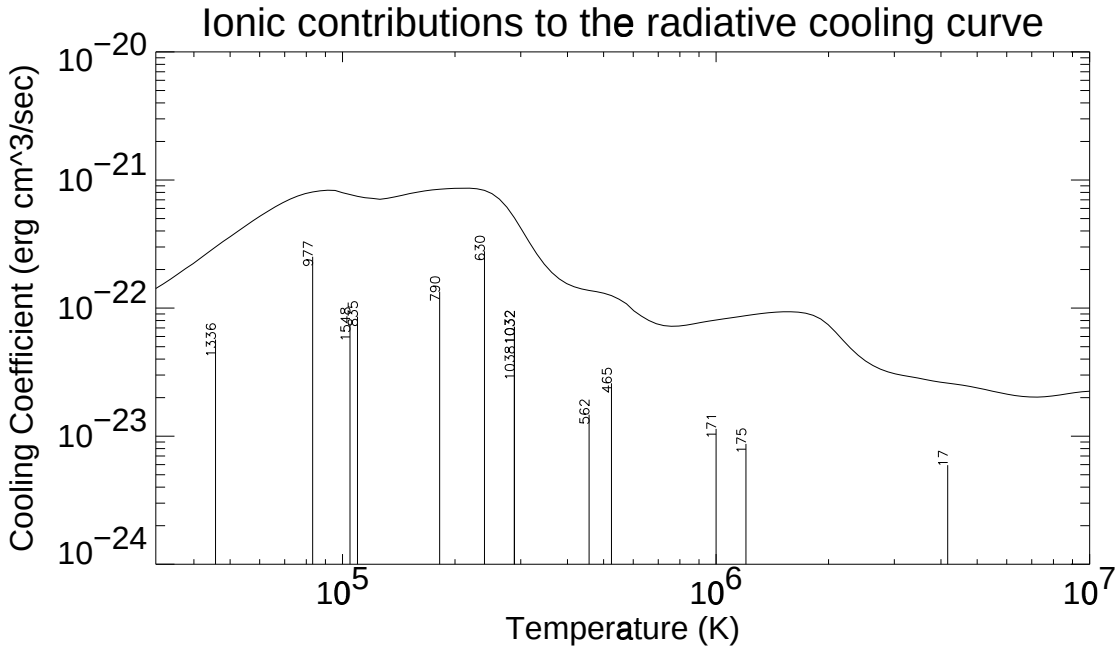

Figure 2.1: Contributions of specific emission lines to the radiative cooling curve

many different ionized species (CIV, SiIV, NV, OVI) share many common characteristics. A highly idealized model of an FUV absorption line is shown in Figure 2.2. These studies show that the absorption lines consist of a few velocity components. Typically the components are dispersed from one another by 30 km/s RMS. For stars in the galactic halo, components at negative radial velocity outnumber those with positive velocity. Occasionally components with infall velocities as high as 125 km/s are seen.

In general, each of the individual components of these absorption profiles is narrow, with widths of about what would be expected for gas at the temperatures where these species would be abundant. This suggests that internal turbulent motions in this gas are not very important.

Unfortunately, the absorption data do not provide much information about the distribution of the absorbing regions along the line of sight. The physical extent of the absorbing regions is a key to differentiating between the models described in

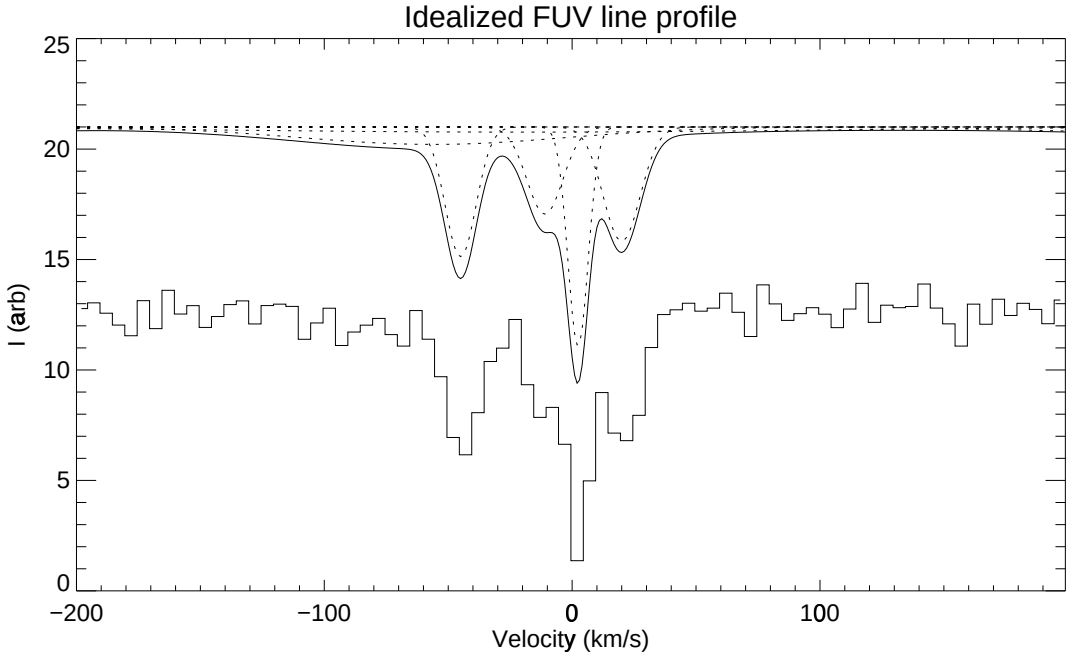

Figure 2.2: An idealized FUV absorption line profile.

Chapter 1.

It should also be noted that these observations are insensitive to any broad components that may exist. Because of their width and the difficulty of separating them from the more easily detected narrow components, broad components could exist in these spectra even though none have been detected. A broad component, with column density equivalent to that of the narrow components, is shown in Figure 2.2 to illustrate the difficulty of detecting these components.

The end result of these ambiguities is that all of the major theories describing the structure of the interstellar medium can be made to fit the existing observations.

2.1.1 Analyses of OVI absorption lines

Initial analysis of the Copernicus OVI measurements was performed by Jenkins and co-workers [23, 24]. They concluded that the OVI absorption features occurred

in clumps of column density about 1×10^{13} cm^{-2} and had a mean line of sight spacing of 165 parsecs. The mean midplane OVI density was determined to be about 2.8×10^{-8} cm^{-3} . Because the observed stars were all near the galactic plane, no accurate scale height for these features could be determined. The observations were consistent with scale heights between 300 and 3000 pc. The small column density and low mean spacing of the features has been said to be most consistent with the McKee-Ostriker model of the ISM.

A recent reanalysis by Shelton and Cox [41] has called these results into question. They added a local component, consistent with the local bubble and its boundaries with cooler gas, into the analysis. Their analysis indicated that a column density of 1.6×10^{13} cm^{-2} is present in all stars more distant than 200 parsecs. This reduces the midplane density of OVI for features outside of the local bubble to about $1.7 \pm 0.4\times10^{-8}$ cm^{-3} . They also find much larger clump densities ($2–7\times10^{13}$ cm^{-2}) and mean line of sight clump spacings (450-1300 pc) than did Jenkins. This would seem to indicate a model where OVI features were much more rare than in the McKee Ostriker model.

2.2 FUV emission measurements

2.2.1 From 1300 Å to 1800 Å

Martin and Bowyer [27] investigated the FUV background between 1300 and 1800 Å using the Space Shuttle-borne UVX experiment. They detected CIV $\lambda\lambda$ 1548,1551 and OIII] $\lambda\lambda$ 1661,1666 emission along several lines of sight. The measured intensity of these lines is plotted versus the galactic latitude of the measurement in Figure 2.3. These lines appeared brighter toward the galactic poles by a factor of at least two. By assuming that the CIV emission was produced by the same gas that produces CIV absorption lines, they calculated a gas density of .005 – .01 cm^{-3} , a pressure of about 1000 cm^{-3} K , and a filling factor of 1 – 10 %. CIV /OIII] ratios point to a gas temperature of about 7.1×10^{4} K . They concluded that these parameters were consistent only with a galactic fountain model of the hot interstellar medium.

More recently Dixon, Davidsen and Ferguson used the Hopkins Ultraviolet Telescope (HUT) to search for FUV emission lines [13]. They determined upper limits to CIV $\lambda\lambda$ 1548,1551 and OIII] $\lambda\lambda$ 1661,1666 along several lines of sight. These limits are consistent with those of Martin and Bowyer at equivalent galactic latitude. Where relevant these upper limits are also shown in Figure 2.3. The results of Dixon *et al.* pertaining to shorter wavelengths are discussed in subsection 2.2.2.

2.2.2 From 900 to 1200 Å

Several attempts have been made to measure diffuse line emission between 900 and 1200 Å . The most successful of these have been Voyager UV Spectrometer measurements by Holberg [19], a sounding rocket observation by Edelstein and Bowyer [15], and measurements made by the Hopkins Ultraviolet Telescope [13]. These measurements are shown in Figure 2.4. Only one of these previous measurements is a detection, that of Dixon *et al.*

The Voyager observations have recently been called into question by Edelstein and Bowyer [15]. Because of the poor resolution of the Voyager spectrometer (> 20Å) the OVI doublet resides well within the core of the Ly β line, making an upper limit determination difficult without major assumptions about the instrument background and line shapes. Edelstein and Bowyer estimate that the upper limits that can be deduced from these data are at least a factor of two higher than those published by Holberg.

The HUT observations of Dixon *et al.* were also made with an instrument with poor spectral resolution ($\simeq$ 10 Å). Their measurements depend greatly on their ability to accurately model the profile of the diffuse Ly β line. They observed ten lines of sight at high galactic latitude and claim detections along four of the ten lines of sight. Unfortunately three of the detections lie within an area of enhanced soft X-ray emission associated with Radio Loop I, a large nearby region of hot gas, therefore it is not known whether these measurements represent the state of hot gas in the galactic halo, or are only indicative of conditions within the Loop I superbubble. The remaining line of sight may be more indicative of the general conditions in the galactic

halo. However, the lack of detections along six fairly nearby lines of sight, some lower than the measurements, could indicate that their measurement is not indicative of conditions in the "typical" diffuse ISM.

Dixon *et al.* determined that the OVI they measured along this line of sight was consistent with temperatures between 2×10^5 and 6×10^5 K, pressures between 2.2×10^4 and 6.7×10^4 cm^{-3} K, and densities near 0.06 cm^{-3}. These parameters are as much as an order of magnitude higher than those determined by Martin and Bowyer's CIV measurements. Therefore they concluded that the OVI they saw was produced by gas that is distinct from that which produces CIV emission.

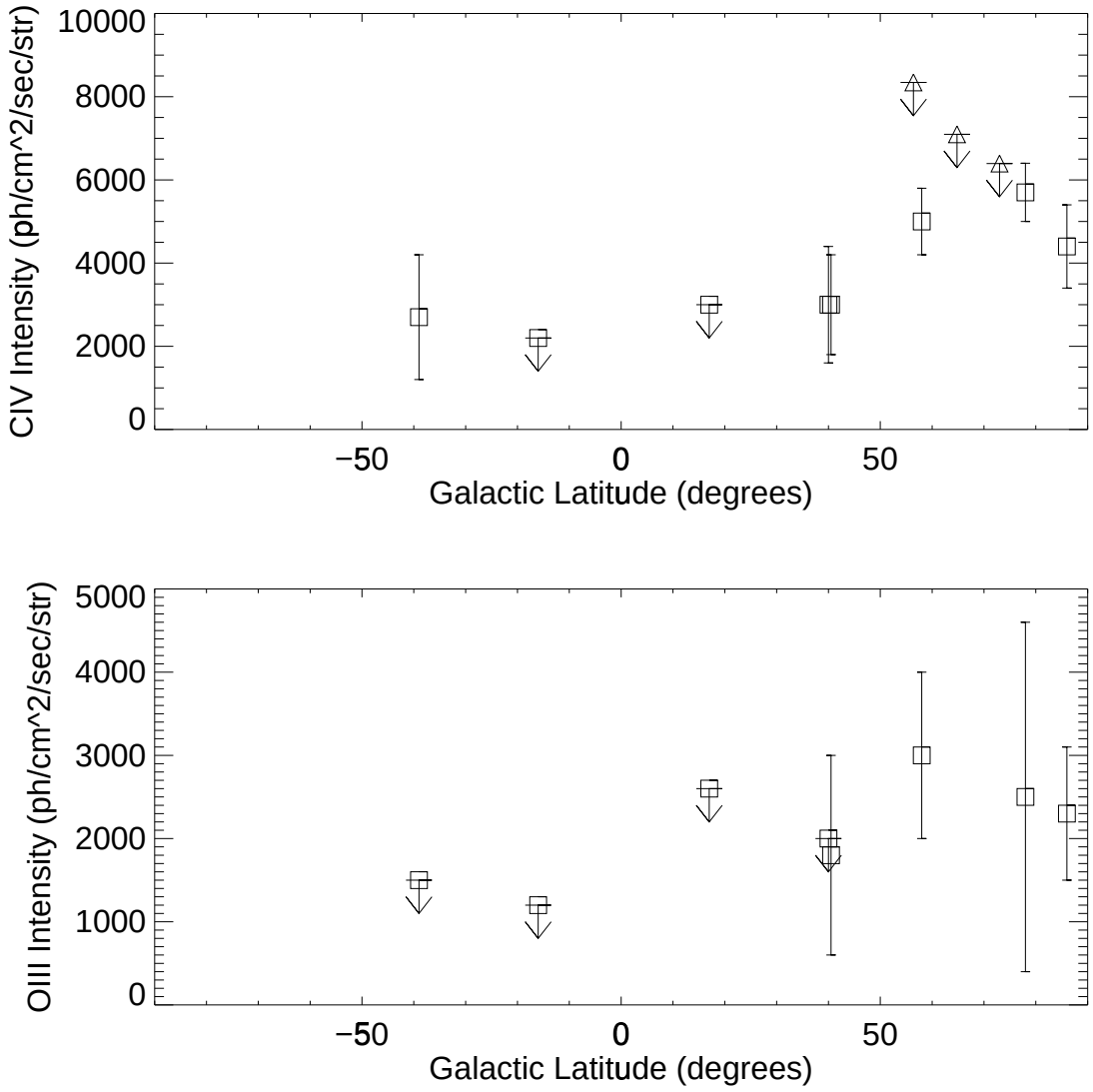

Figure 2.3: Measurements of diffuse CIV and OIII] line emission. Measurements by Martin and Bowyer are shown as squares. Measurements by Dixon *et al.* are shown as triangles.

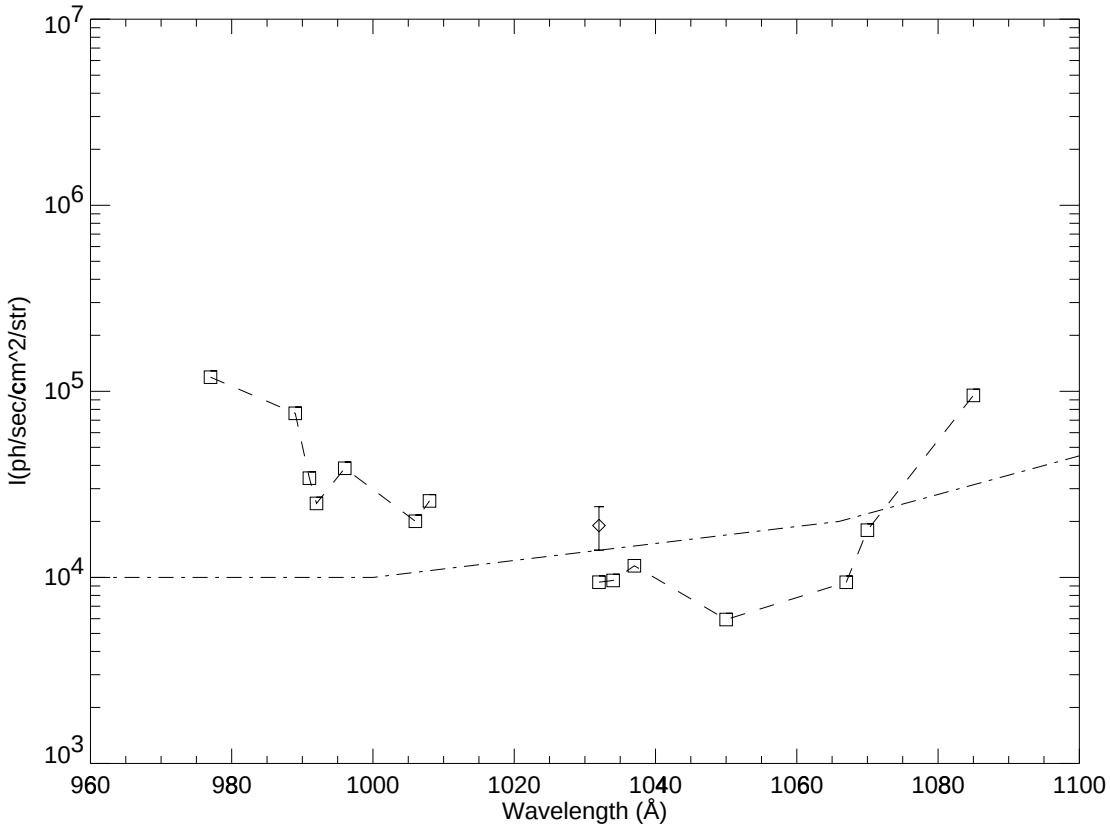

Figure 2.4: Previous measurements of FUV line emission between 900 and 1200 Å . Limits by Edelstein and Bower are shown as squares. Limits by Holberg are shown as the dot-dashed line. A measurement by Dixon *et al.* is shown as the diamond.

Chapter 3

The DUVE Instrument

Because of the importance of the OVI $\lambda\lambda$ 1032,1038 lines in the diffuse interstellar medium, it was decided that the DUVE spectrometer would primarily target these lines. Because of the close proximity of the bright Ly β λ 1025 airglow line, a high resolution instrument is required for detection of the OVI lines. A small bandpass (150 Å) around these lines would also include the potentially important CIII λ 977, NIII λ 991, and CII λ 1037 lines. Many problems need to be solved in the design of a diffuse spectrometer for this bandpass. The low intensity of the emission lines I am attempting to detect requires that the spectrometer have a high effective area $\times$ solid angle product. In addition, sources of instrument background and spectral contamination must be limited.

3.1 Potential sources of background and spectral contamination

3.1.1 Atmospheric airglow

There are several bright airglow lines which could interfere with attempts to observe the OVI $\lambda\lambda$ 1032,1038 lines. The nearest lines HI λ 1025, and OI λ 1027 have a combined intensity of about $10^{5.5}$ ph s^{-1} cm^{-2} str^{-1} . Assuming Gaussian line profiles, it can be shown that a 2.7 Å HEW is required if the contribution to a bin at 1032 Å

is to contain less than 5000 ph s^{-1} cm^{-2} str^{-1} equivalent background due to these lines. For this reason, high spectral resolution is required to prevent contamination of the faint interstellar emission lines.

Even more troubling is the far brighter Ly α line at 1216 Å . At an intensity of 5 kiloRaleighs (4×10^8 ph s^{-1} cm^{-2} str^{-1}), scattering from optical surfaces could easily swamp any signals. Ly α photons have to be rejected to a level of 5×10^{-6} per spectral bin or less. Unfortunately no filter material exists which is able to block Ly α while allowing OVI $\lambda\lambda$ 1032,1038 to pass through. Less obvious filtering techniques are required.

3.1.2 Intrinsic detector background

Due to efficiency, availability and resolution, microchannel plate detectors were chosen to be used in this instrument. There are two roughly equal components to the intrinsic background found in microchannel plate detectors, cosmic rays and radioactive decay of potassium in the plates. Each is present at a rate of about 0.5 counts/second per square centimeter of detector surface.

It is possible to eliminate cosmic ray counts by using an anti-coincidence detector surrounding the microchannel plate, but because the radioactive decay counts are present at the same rate it was not considered to be worth the time and cost involved.

Recently, microchannel plates manufactured without the use of potassium have become available. Unfortunately they were not available at the time the DUVE experiment was being designed and assembled.

3.1.3 Stellar contamination of diffuse spectra

Another potential background in the diffuse spectrum is stellar contamination. We can divide this category into two subcategories: 1) bright O, B, and A stars in the field of view and 2) unresolved stars.

The first of these problems can be solved by not pointing the instrument near any known bright stars that could have large FUV fluxes. In addition, the instrument can be designed so as to limit the fraction of the detector area on which light from a

single star will land. This is, in general, accomplished by allowing imaging along the spectrometer slit.

The second problem is more difficult to solve. In the case of the DUVE instrument, I used an additional detector providing an FUV image of the spectrometer field. This would allow detection of stars too faint to be seen directly in the spectra and eliminate potentially contaminated data. Even this measure does not guarantee the elimination of general stellar contamination.

3.1.4 Exospheric charged particles

The portion of the background due to exospheric charged particles is potentially quite substantial. This background can range from 1 $s^{-1}cm^{-2}$ to upwards of 10^5 $s^{-1}cm^{-2}$ for an open faced microchannel plate. It is highly dependent on orbital parameters, especially ram angle, solar angle, altitude and position over the earth's surface.

At other wavelengths, it is possible to create an enclosed detector with a filter over the entrance aperture. Lack of filters for this bandpass made this impossible for the DUVE instrument.

Wire screens charged to potentials above the thermal energy of the charged particles can be employed over detector faces and entrance apertures. A positively charged grid will impede the progress of protons and positive ions. Past experience has shown these barriers to have minimal effectiveness.

Another possibility for controlling this background is "magnetic brooms" near entrance apertures and slits which attempt to direct charged particles toward a grounded surface.

Both of these control methods were used in the DUVE spectrometer in an attempt to limit this background. In addition, shutter closed observations were made in flight to allow calibration of the entire non-photonic background. In flight, overall background rates varied and ranged from 1 $s^{-1}cm^{-2}$ (near zero charged particle background) to 20 $s^{-1}cm^{-2}$ with a median value of 2 $s^{-1}cm^{-2}$, indicating that these control methods were quite successful. Overall, our measured backgrounds consisted

of roughly equal parts charged particle background and intrinsic detector background. No scattered Ly α was detected.

3.2 Design of the DUVE spectrometer

The design of the DUVE instrument is a reworking of a design by Edelstein [15]. The design is a two stage spectrometer which solves many of the above background problems yet provides an large area $\times$ solid angle product when compared to alternative designs. A schematic of the instrument is shown in Figure 3.1.

3.2.1 The filtration stage

The purpose of the first stage of the spectrometer is to filter out unwanted wavelengths, especially Ly α λ 1216. Light entering the spectrometer passes through a wire grid collimator with a full width of $\pm 1°$. The entrance aperture is covered with a fine mesh charged to +28 Volts in an attempt to limit the number of exospheric electrons that enter the instrument. After passing through the collimator, the light strikes a diffraction grating in Wadsworth configuration. Wadsworth configuration describes a spectrometer consisting a spherical, toroidal, or parabolic optic which focuses the spectrum of an infinitely distant object onto a slit or detector at a finite distance. In this case first order light from the grating is focused toward a slit.

Contrary to intuition, the slit does not limit the instrument bandpass. Using Fermat's principle we can reverse the light path. If a non-monochromatic source were placed at the slit of the instrument, each wavelength would diffract from the grating at a different angle. Only those with a specific range of wavelengths could pass through the collimator. Thus it is the collimator width and the grating ruling density that define the width of the instrument bandpass. Each individual wavelength accepted by the slit has entered the collimator at a slightly different angle. This has the unique advantage of limiting contamination by a bright star to a wavelength range much smaller than the overall bandpass. The overall bandpass is adjusted by Wadsworth line spacing and incidence angle. The slit width defines the horizontal (across the slit)

Figure 3.1: A schematic of the DUVE instrument.

Wadsworth Grating Parameters	
Line density:	2400 $mm^{-}1$
Ruling type:	Holographic
Radius of curvature:	375 mm
Spectral focus distance:	190.5 mm
Exit Slit Width:	0.5 mm = 0.143 °
Central wavelength[1]:	1009 Å
Incident angle at central λ [1]:	14.14 °
Diffraction angle[1]:	0.16 °
Full bandpass[1]:	938-1080 Å

Table 3.1: Wadsworth grating parameters

[1] As installed.

acceptance angle and the resolution of the second stage of the instrument. Table 3.1 shows the parameters of the spectrometer filter stage.

In order to detect stars that might enter the field of view, zero order light from the Wadsworth grating is focused onto a microchannel plate detector. The detector is covered by a BaF window which effectively filters out wavelengths shorter than 1300 Å . The result is an FUV image of the sky taken through the entrance aperture.

In addition a shutter is centered in the light path just in front of the slit. This shutter toggles its state approximately every 16 seconds during observations. This allows accurate in-flight determination of the non-photonic background.

3.2.2 The dispersion stage

The second stage of the spectrometer is the dispersion stage. Light entering through the slit strikes a diffraction grating in a Rowland circle configuration. In a Rowland circle configuration both the source (entrance slit) and spectral focus (detector) are at finite distance from the optical surface. A solution of the grating equation for a spherical optic requires that both lie on a circle with a diameter equal to the grating radius of curvature which lies tangent to the grating center. Second order diffracted light of the appropriate bandpass strikes a microchannel plate detector. Spectral resolution of the second stage is determined by properties of the diffraction

Rowland Spectrometer Parameters	
Line density:	2950 $mm^{-}1$
Ruling type:	Holographic
Radius of curvature:	375 mm
Entrance slit distance:	347 mm
Entrance slit width:	0.5 mm = 2.4 Å
Spectral focus distance (1032 Å):	365 mm
Incident angle:	-22.3 °
Diffraction order:	-2
Diffraction angle (1032 Å):	-13.2 °

Table 3.2: Rowland spectrometer parameters

grating and the width of the entrance slit. Table 3.2 shows the parameters of the spectrometer dispersion stage.

Unwanted orders are blocked in this stage of the spectrometer through use of strategically placed baffles. They are specifically designed to eliminate all orders of Ly α λ 1216 which may have been scattered through the entrance slit.

Use of second order light in the diffraction stage allows high dispersion without significantly increasing the line density required to achieve the required spectral resolution.

Both stages of the spectrometer have been designed to allow imaging along the slit. In calibration, the optical imaging resolution was shown to be about 4 arcminutes. Unfortunately, constraints of image storage electronics reduce this resolution to 10 arcminutes in practice.

3.3 Grasp calibrations

The count rate signal (C) observed by a photon counting instrument observing a diffuse emission line is given by the the intensity of the line ($I(\lambda)$) multiplied by the instrument quantum efficiency ($\varepsilon(\lambda)$) integrated over the geometric area of the

instrument ($dA(\lambda)$) and the geometric solid angle ($d\Omega(\lambda)$).

$$C = \int\int I(\lambda,\theta,\phi)\cdot\varepsilon(\lambda,\theta,\phi,x,y)dA(\lambda,\theta,\phi)d\Omega(\lambda)$$

In principle, both the aperture and angular limits can have wavelength dependence that is independent of the instrument quantum efficiency, but in practice these effects can be folded into the quantum efficiency term. In the case of uniform intensity over the aperture and solid angle, the line intensity can be removed from the integral and the result expressed as

$$\frac{C(\lambda)}{I(\lambda)} = \overline{\varepsilon}(\lambda)\cdot A_{\rm geom}(\lambda)\cdot\Omega_{\rm geom}(\lambda)$$

where $\overline{\varepsilon}$ is the instrument quantum efficiency averaged over the geometric area and solid angle (effective quantum efficiency), $A_{\rm geom}$ is the geometric area and $\Omega_{\rm geom}$ is the geometric solid angle. This effective (efficiency$\times$area$\times$solid angle) product is known as the instrument grasp. In general, the effective quantum efficiency can be expressed as the product of several components which can be measured or calculated. In the case of the DUVE instrument this equations expands to

$$\frac{C(\lambda)}{I(\lambda)} = \left[\varepsilon^{(0,0)}_{\rm collimator}(\theta(\lambda))\right]\left[\varepsilon^{(0,0)}_{\rm optics+mcp}(\lambda)\right]\left[\frac{\overline{\varepsilon}}{\varepsilon^{(0,0)}_{\rm optics+mcp}}(\lambda)\right]$$

$$[A_{\rm geom}]\left[\overline{V}_\theta(\lambda)\Delta\theta_{\rm geom}(\lambda)\right]\left[\overline{V}_\phi(\lambda)\Delta\phi_{\rm geom}(\lambda)\right]$$

where each term in brackets is measured or calculated independently. A discussion of the first three terms is given in the subsection on quantum efficiency calibration. The fourth and fifth terms are discussed in the subsections on geometric area calibration and solid angle calibration respectively.

3.3.1 Quantum efficiency calibration

The quantum efficiency of the DUVE instrument has several contributions.

1. The transmission of the wire grid collimator vs angle ($\varepsilon^{(0,0)}_{\rm collimator}(\theta)$) was measured using a Ly β λ 1025 pencil beam. The resulting measurements were then fit to a model of expected collimator transmission. The resulting transmission

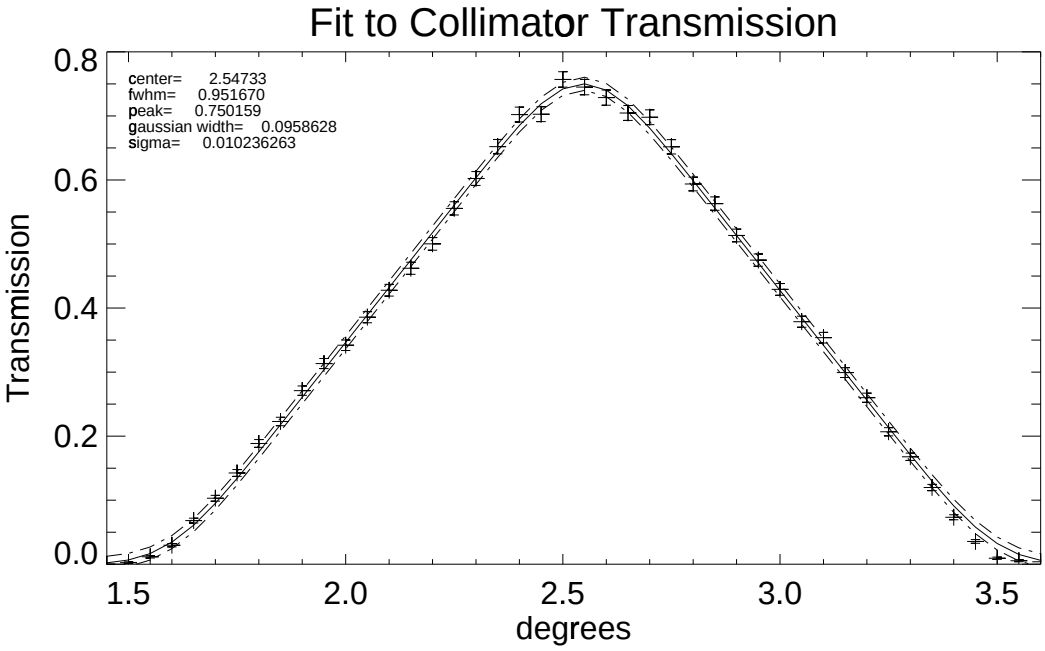

Figure 3.2: Collimator transmission and best fit model.

λ (Å)	Quantum Efficiency
972.5	$2.9 \pm 0.3 \times 10^{-4}$
988.8	$4.4 \pm 0.4 \times 10^{-4}$
999.	$5.8 \pm 0.6 \times 10^{-4}$
1025.7	$1.5 \pm 0.1 \times 10^{-3}$
1027.4	$1.5 \pm 0.1 \times 10^{-3}$
1048.2	$1.8 \pm 0.2 \times 10^{-3}$
1066.7	$1.9 \pm 0.2 \times 10^{-3}$
1086.	$2.6 \pm 0.3 \times 10^{-3}$

Table 3.3: Combined optical and spectral detector quantum efficiency at grating center.

profile, shown in Figure 3.2, was very close to the collimator's design parameters of 75% peak transmission and 1 ° FWHM. Entrance angles were measured using an encoded rotation stage. Fractional transmission was measured using comparisons of count rates on a microchannel plate detector with the collimator in the beam and with the collimator removed from the beam.

2. The efficiency of the optics and microchannel plate detectors ($\varepsilon^{(0,0)}_{\mathrm{optics+mcp}}(\lambda)$) were measured at eight wavelengths. These measurements were made with the optics in place in the instrument, but with the slit and collimator removed. A narrow beam was used and the measurements were taken with the beam striking the center of the Wadsworth grating. Source flux was determined using an NBS calibrated FUV photodiode. The results of these measurements are shown in Table 3.3. A model based upon expected quantum efficiency of the gratings and detector used was fitted to these measurements.

3. Efficiency measurements relative to efficiency at grating center were made at a grid of pencil beam positions on the Wadsworth grating at each wavelength. This allowed a correction to be made for efficiency averaged over the grating surface. The ratio of average quantum efficiency to central quantum efficiency ($\frac{\overline{\varepsilon}}{\varepsilon^{(0,0)}_{\mathrm{optics+mcp}}}$) was determined to be .82$\pm$.05 and shown to have very little variation with wavelength.

4. The slit was placed in the instrument and angular sweeps were made to both determine the angular focus width of the Wadsworth grating at the slit and to provide verification of the angular width of the slit. The focus was shown to have an angular Gaussian width of $2.2 \pm 0.3 \times 10^{-2}$ ° with minimal variation with wavelength. The angular full width of the slit was shown to be $1.43 \pm 0.05 \times 10^{-1}$ ° . Thus it was concluded that light loss due to focus effects was minimal and that the full angular width of the slit could be used for solid angle calculations.

5. The collimator was installed. Its angular center was ascertained by determining the angle at which the count rate on the zero order detector was maximized. This was shown to place the maximum collimator throughput at a wavelength of 1009.0 ± 1.8 Å .

6. I combined models of collimator throughput and combined optics and detector efficiency and performed an analysis of potential errors in measured quantum efficiency and collimator alignment. The results of this analysis are shown in Figure 3.3.

3.3.2 Geometric area calibration

The Geometric area of the spectrometer (A_{geom}) is defined by the size of the spectrometer entrance aperture, which is a circular opening 7.5 cm in diameter. Corrections for vignetting ($\overline{V}_{\phi,\theta}$) due to field restrictions in the collimator, slit, detectors and baffles will be discussed in the section on solid angle calibration.

3.3.3 Solid angle calibration

The calibration of the instrument's solid angle was more difficult. This measurement includes vignetting effects in both the vertical (along the slit) and horizontal (across the slit dimensions).

The effective vertical acceptance ($\overline{V}_{\phi}\Delta\phi$) is limited by several items: 1) the angular height of the slit, 2) the angular height of the detector, and 3) vignetting due to

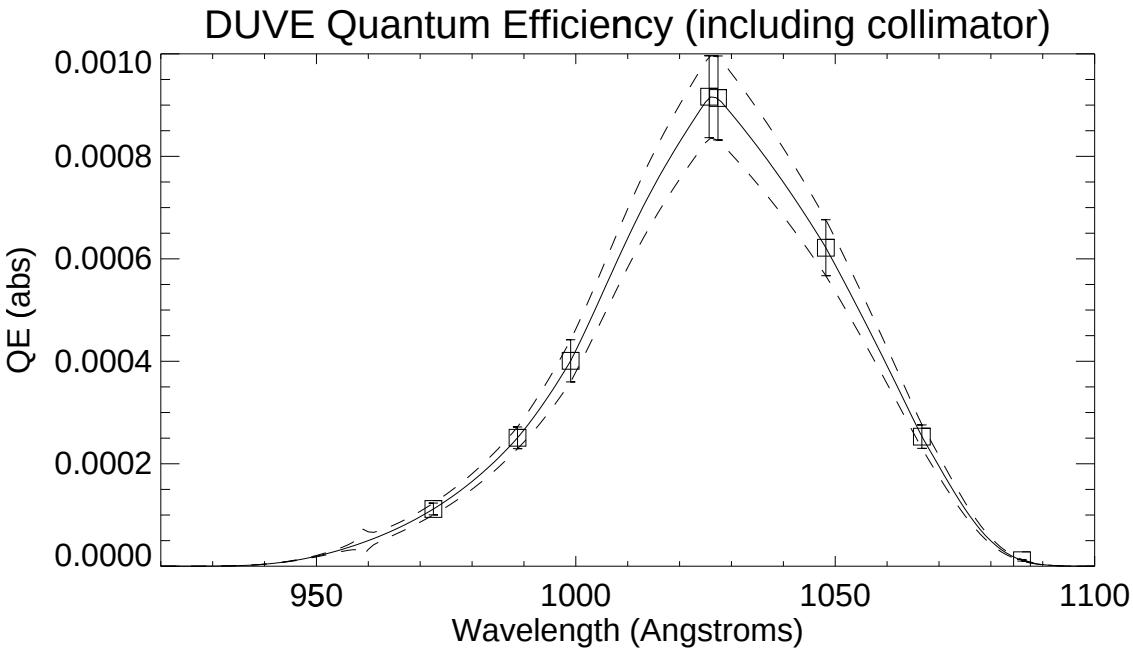

Figure 3.3: DUVE overall quantum efficiency.

collimator cross bars and aperture limits. All of these items can be calculated from design parameters and were verified by measurement during calibration. The verifications were made by directing a wide collimated beam through the entrance aperture and measuring variations in the detector count rates with pitch angle. These measurements were made at three wavelengths. The difference between the measurements and geometrically calculated values is within the measurement errors.

The effective horizontal acceptance could not be directly measured in the instrument and had to be computed. The main limiting factors in the horizontal acceptance are the slit width and vignetting due to the entrance angle at various wavelengths. It can be easily shown that the effective horizontal acceptance (ignoring the effects of the collimator which are included in the quantum efficiency calculation) at a given wavelength is:

$$\overline{V}_\theta \Delta\theta = \int_{-\frac{w}{2}}^{\frac{w}{2}} (1 - \mid \tan(\theta_\lambda + x) \mid) \, dx$$

where w is the angular width of the slit and θ_λ is the angle at which the wavelength enters the collimator. Given the central collimator wavelength (1009 Å), the slit width (.143 °), the angular dispersion of the grating (measured 72.8 Å per degree), and the small angle approximation, this reduces to:

$$\overline{V}_\theta \Delta\theta = \left(0.143 - 3.4 \times 10^{-5} \mid \lambda - 1009 \text{ Å } \mid\right)^\circ$$

Again using the small angle approximation, the horizontal and vertical acceptance can be multiplied to give solid angle acceptance. A plot of solid angle acceptance versus wavelength is shown in Figure 3.4. Multiplying the effective solid angle, the geometric area, and the quantum efficiency gives us the product shown in Figure 3.5.

3.4 Spectral resolution calibration

To determine spectral resolution, a pencil beam of light from a non-monochromatic gas discharge source was used. Because of the wide field of view and the wavelength dependent nature of the entrance angle, the instrument was rotated around an axis parallel to the slit during the measurements. The measurement was repeated at several vertical entrance angles (ϕ) to accurately calibrate variations along the length

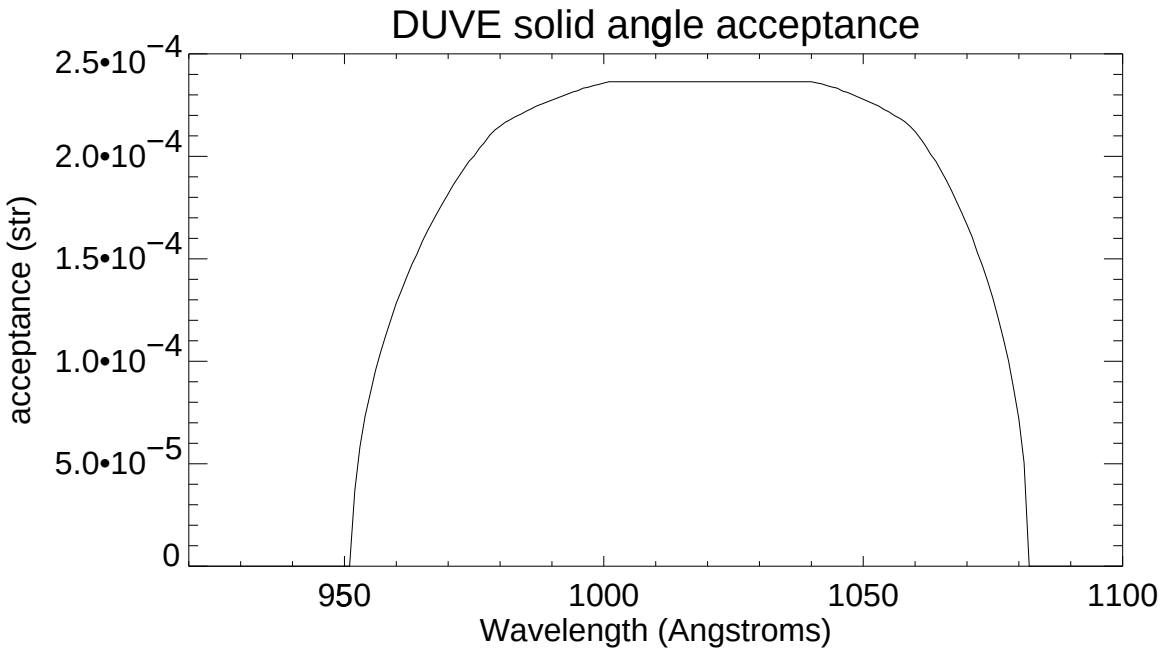

Figure 3.4: DUVE solid angle acceptance

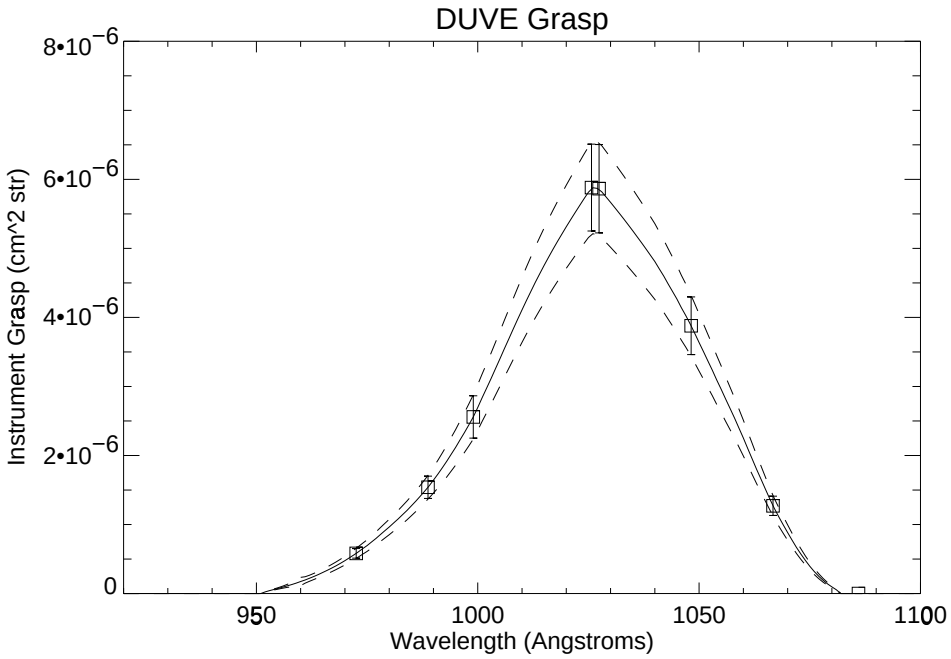

Figure 3.5: DUVE area solid-angle product

of the slit. This had the added benefit of providing a (ϕ, λ) to detector (x, y) position mapping function for use in correcting optical and detector distortions using a polynomial image warping technique.

After applying the warping technique, the instrument was found to have a HEW of 3.5 Å at Ly β . However, because the line profile asymmetric with a much steeper cut-off toward long wavelengths, it has the same contribution at 1032 Å as an equivalent line with an HEW of 2.3 Å .

3.5 Data accumulation and format

The DUVE instrument contains an on board memory which accumulates images of the detector fields. The instrument memory is sufficient to hold eight shutter open spectral detector images, eight shutter closed spectral detector images, eight zero order detector images, and 1748 seconds of instrument health data. The spectral detector images have a resolution of 256 (spectral) by 32 (along slit) by 16 bits. Zero order detector images are 32 by 64 by 16 bits. During normal operations, the images are accumulated for 218.5 seconds each, half of which is shutter closed time. Instrument health data is sampled at a rate of 16 bits per 0.21 seconds.

Telemetry consist of a continuous memory dump over a single (bi-phase level) serial line, at a rate of 4800 bps. A full memory dump takes 305 seconds. Memory is dumped continuously during instrument operation.

3.6 Flight parameters and instrument operations

The DUVE instrument was launched as a secondary payload attached to the second stage of a Delta II 7925 vehicle on 24 July, 1992. (Figure 3.6) As a secondary payload, the parameters of the DUVE orbit were determined by the requirements of the primary payload, the Geotail satellite. Fortunately the parameters required by Geotail resulted in an excellent orbit for diffuse observations. A morning launch resulted in a near midnight apogee of 1460 km (750 nmi). This placed the instrument

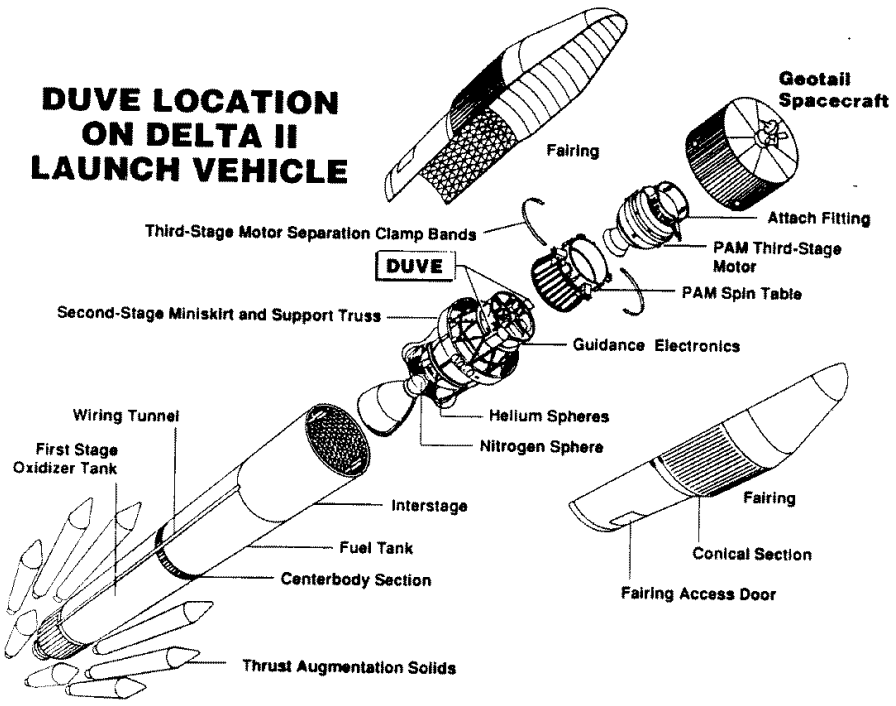

Figure 3.6: Location of the DUVE instrument on the Delta II Launch Vehicle (courtesy McDonnell Douglas Space Systems Company)

well above the majority of atomic oxygen airglow and above about half of the expected geocoronal hydrogen airglow.

Due to safety requirements, the propellant and control gases of the second stage had to be depleted by the end of the first orbit. Therefore the mission was conducted in two phases, a pointed phase and a spin stabilized phase. Because the DUVE data was telemetered through the second stage telemetry system, the mission lifetime for DUVE was limited by the battery power available to the telemetry system (about 8 hours total).

3.6.1 The pointed phase

During the first orbital night, the instrument was pointed at the primary target and a slow drift (0.1 $^{\circ}$ min^{-1} perpendicular to the slit) was initiated. This phase continued until T+5000 seconds, at which time second stage depletion and spin up were begun. Observations continued throughout the depletion period. However, much of the data was contaminated by stars and bright airglow.

3.6.2 The spin stabilized phase

Before the control gases were depleted, the stage was pointed and spun at a rate of 30 degrees/second. The vehicle was pointed such that expected atmospheric torques would bring the stage back toward the primary target for the third orbital night. Because the stage was not spin balanced, the field of view was not aligned with the axis of the spin, but was offset by about 7 degrees. This increased the susceptibility to contamination by bright FUV sources.

The second phase continued until the depletion of the stage telemetry system battery at T+30,000 seconds.

Chapter 4

Data Analysis

4.1 Image selection

Detector images telemetered from the spacecraft were stored on magnetic tape for later analysis. Because the images were telemetered multiple times over many ground station passes, many data dropouts were able to be corrected. The end result was 19 images representing 4151 seconds of observation time. These images were examined for stellar contamination, uncorrected data dropouts and instrument anomalies. Where possible, these portions of the image were masked off or otherwise corrected. Where no correction was possible, the images were discarded. The corrected images were sorted in order of background (shutter closed) count rates as a means of determining which represented low noise observing periods.

To determine which images were to be used for the analysis, only low noise images were considered. The images were ordered in order of background level. It was determined whether adding the next higher background image to the low noise set would increase the overall signal to noise level. Fifteen of the images passed this test. The background level of those that were chosen ranged from 1.0 to 2.6 cm^{-2} s^{-1}. The background levels of those rejected were from 8.2 to 20 cm^{-2} s^{-1}. The resulting image sum of the accepted images is shown in Figure 4.1. The top image is a sum of shutter opened images. The vertical stripe is Ly β λ 1025 airglow. The bottom is a sum of shutter closed images. The image has not been corrected for distortions.

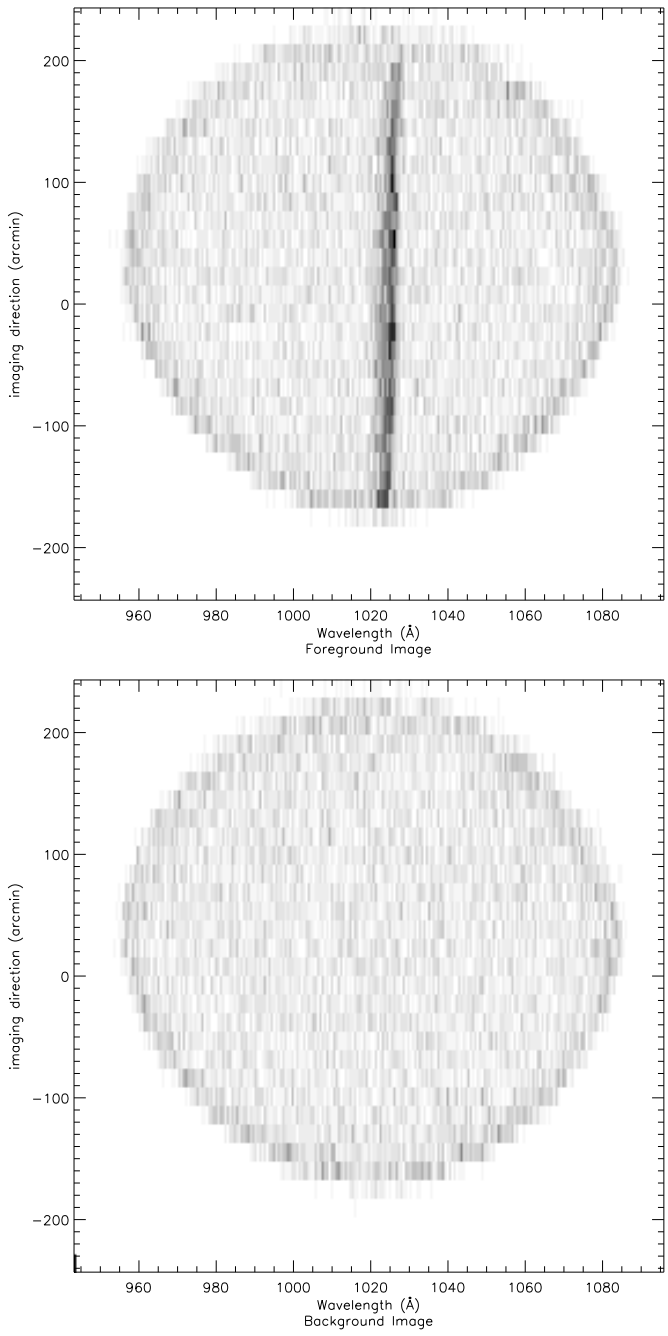

Figure 4.1: Raw spectral detector images from the DUVE instrument's flight. The top image is a sum of shutter opened images. The vertical stripe is Ly β λ 1025 airglow. The bottom is a sum of shutter closed images. Image is not corrected for distortions.

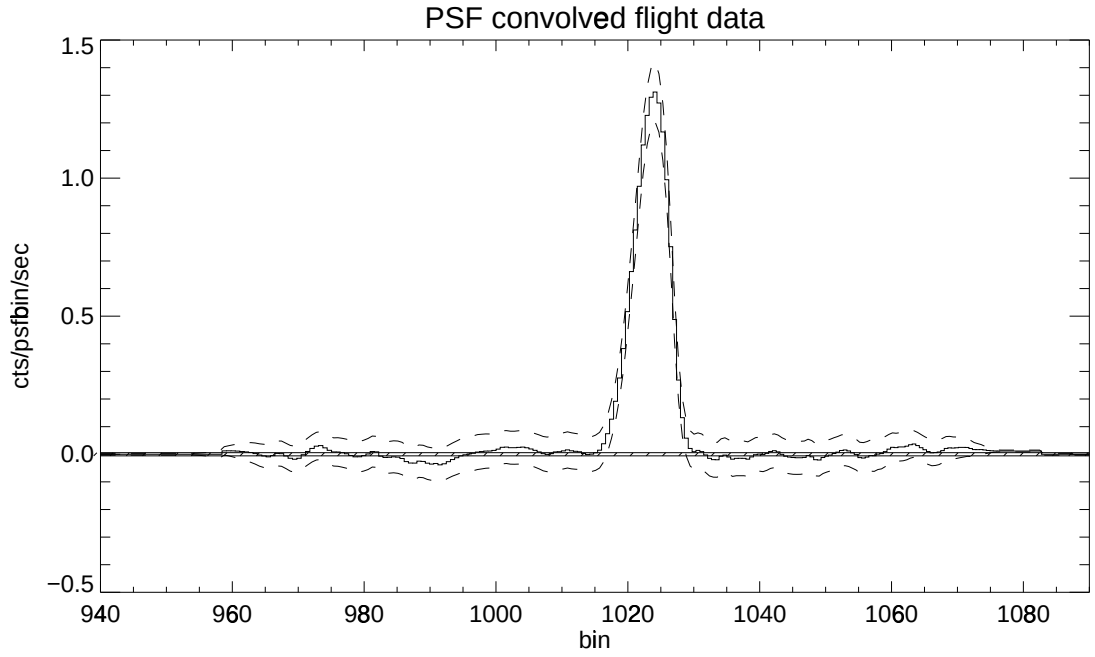

Figure 4.2: Flight spectral data after convolution with a line spread function

4.2 Emission line limits

The resulting images were corrected for image distortions and shutter open/closed time, and the background image was subtracted from the foreground. The resulting image was histogrammed and convolved with a line spread function that was determined during calibration. The convolved histogram is shown in Figure 4.2. The dashed lines represent $\pm 3\sigma$ error levels as determined through count statistics and potential error in the determination of shutter open/closed time. This quantity is determined by the following formula.

$$\sigma = \sqrt{\sigma_{\rm fg}^2 + \sigma_{\rm bg}^2 + \sigma_{\Delta t}^2}$$

$$= \sqrt{\left(\frac{N_{\rm fg}}{t_{\rm fg}}\right)^2 + \left(\frac{N_{\rm bg}}{t_{\rm bg}}\right)^2 + \left(\frac{N_{\rm fg}\Delta t}{t_{\rm fg}^2} + \frac{N_{\rm bg}\Delta t}{t_{\rm bg}^2}\right)^2}$$

The quantities $N_{\rm fg}$ and $N_{\rm bg}$ are the number of counts (post-convolution) per wavelength bin in the foreground and background images respectively. The values $t_{\rm fg}$ and $t_{\rm bg}$ represent the shutter open and shutter closed integration times (1582.6 and

1529.2 s) and Δt represents the uncertainty in those times (14.0 s). The hatched area near the baseline in Figure 4.2 represents the approximate fraction of the error that is due to potential errors in shutter timing.

It can easily be seen that only one spectral line exceeds the 3σ significance level. That line is the aforementioned geocoronal Ly β λ 1025 line. By dividing the count rate in this line by the DUVE grasp, I determined its intensity. The 1.31 counts per second detected corresponds to an intensity of $2.26 \pm 0.26 \times 10^5$ ph s^{-1} cm^{-2} str^{-1}. As expected this value is between that measured at low altitude (600 km) [6] and the interplanetary value [19].

As a statistical test of the error levels, fluctuations in the spectrum outside of the 1025 Å line were compared with those expected by statistics. A histogram of the values of $\frac{\Delta n}{\sigma}$ was best fit by a Gaussian of width 1.01 ± 0.03 centered at 0.1 ± 0.1.

Although no other lines were detected, it is possible to use the DUVE data to put upper limits to line emission in this band. Table 4.1 and Figure 4.3 show 90% confidence (1.64 σ) limits to line emission for important lines in this band.

4.3 Continuum limits

Because the error in zero level is correlated over all wavelength bins, it represents the dominant source of uncertainty in the determination of the continuum limits. The contribution of this error is linear in the number of bins included, whereas the errors due to count statistics tend toward the square root of the number of bins. The best determinations of continuum level were $-1.07 \pm 0.69 \times 10^3$ ph s^{-1} cm^{-2} str^{-1} Å^{-1} between 977 and 1020 Å and $-3.2 \pm 3.8 \times 10^2$ ph s^{-1} cm^{-2} str^{-1} Å^{-1} between 1028 and 1057 Å . These measurements allow me to place 2σ upper limits in these ranges of 310 and 440 ph s^{-1} cm^{-2} str^{-1} Å^{-1} respectively.

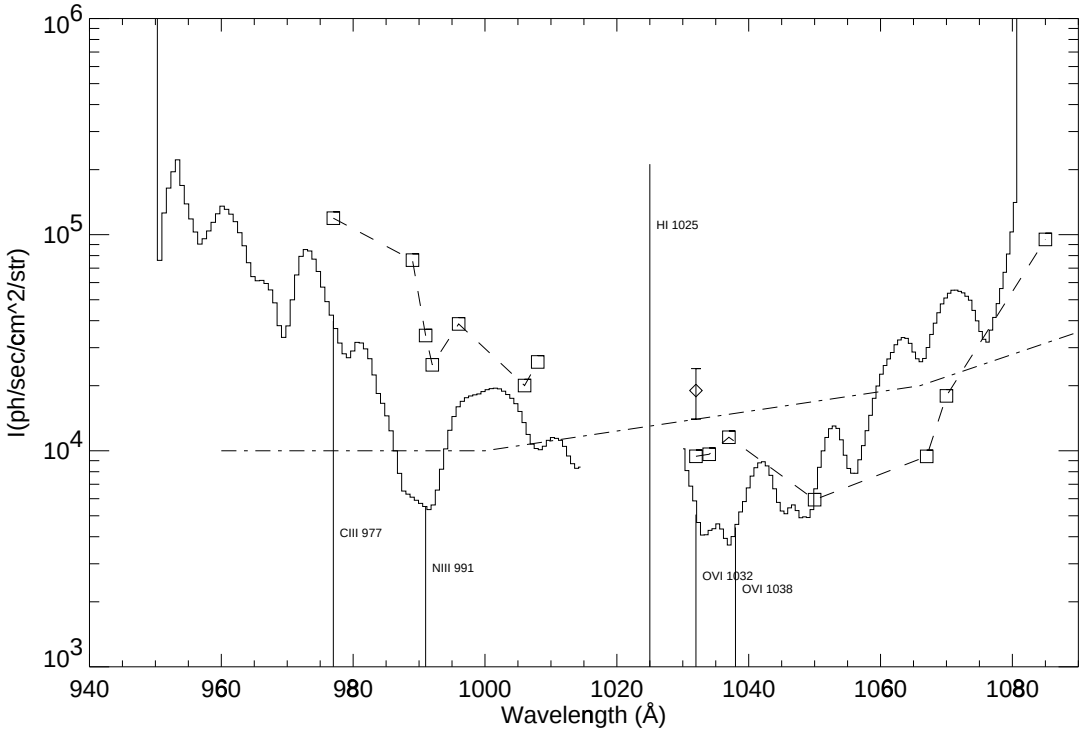

Figure 4.3: Upper limits to line emission placed by the DUVE experiment.

Species	λ(Å)	I(ph s^{-1} cm^{-2} str^{-1})	I(erg s^{-1} cm^{-2} str^{-1})
HI [1]	972	$\leq 7.4\times10^{4}$	$\leq 1.5\times10^{-6}$
CIII [2]	977	$\leq 4.0\times10^{4}$	$\leq 8.1\times10^{-7}$
OI [1]	989	$\leq 6.1\times10^{3}$	$\leq 1.2\times10^{-7}$
NIII [2]	991	$\leq 5.5\times10^{3}$	$\leq 1.1\times10^{-7}$
SiII	992	$\leq 5.7\times10^{3}$	$\leq 1.1\times10^{-7}$
SiIII	996	$\leq 1.6\times10^{4}$	$\leq 3.2\times10^{-7}$
NeVI	1006	$\leq 1.3\times10^{4}$	$\leq 2.6\times10^{-7}$
ArVI	1008	$\leq 1.0\times10^{4}$	$\leq 2.0\times10^{-7}$
HI [1,3]	1025	$2.26\pm0.26\times10^{5}$	$4.38\pm0.49\times10^{-6}$
OVI [2,4]	1032, 1038	$\leq 7.6\times10^{3}$	$\leq 1.4\times10^{-7}$
CII [2]	1037	$\leq 3.9\times10^{3}$	$\leq 7.4\times10^{-8}$
ArI [1]	1050	$\leq 6.4\times10^{3}$	$\leq 1.2\times10^{-7}$
SiIV	1067	$\leq 2.9\times10^{4}$	$\leq 5.4\times10^{-7}$
SIV	1070	$\leq 5.1\times10^{4}$	$\leq 9.5\times10^{-7}$

Table 4.1: Upper limits to line emission placed by the DUVE data

[1] Anticipated airglow line

[2] Constrains state of hot interstellar medium

[3] Detected at 37σ.

[4] This limit is total emission from the doublet based upon joint statistics by assuming $\frac{I(1032)}{I(1038)} = 2$. Upper limits for the individual components of the doublet are $I(1032) \leq 5400$ ph s^{-1} cm^{-2} str^{-1} and $I(1038) \leq 4400$ ph s^{-1} cm^{-2} str^{-1} .

Chapter 5

Isothermal and Evolutionary Models

5.1 Isothermal models

The simplest (and most often used) model of emission from the warm and hot phases of the interstellar medium is that of an optically thin, isothermal, collisionally excited plasma. This simple model does not take into account how the plasma was heated, nor any temperature variations within the plasma as it cools. For an emission line from a specific transition ($k \rightarrow j$) from an ion i the emitted intensity I_{kj} is:

$$I_{kj} = \int_0^\infty \int_0^\infty j_\nu d\nu dx = h\nu_{kj} \int_0^\infty n_i n_e \gamma_{kj} dx$$

where n_i is the density of the ion i in the plasma and n_e is the electron density. The quantity γ_{jk} represents the collision strength into level k and the probability of decay into level j. Determining this quantity is a complicated quantum mechanical calculation and the subject of numerous papers. For the purposes of this discussion values from Landini and Monsignori-Fossi have been used [26]. For an isothermal plasma the above equation can be further reduced to:

$$I_{kj} = h\nu_{kj} \frac{n_i}{n_{\rm HI}} \frac{n_{\rm HI}}{n_e} \gamma_{jk} \int_0^\infty n_e^2 dx$$

The quantities $\frac{n_i}{n_{\rm HI}}$ and $\frac{n_{\rm HI}}{n_e}$ can be determined from the Saha equation by assuming a temperature, density, and elemental abundances for the plasma. If the intensity I_{kj} is

measured and a temperature is assumed, only the value of the integral (known as the emission measure) is left as a free parameter. In practice, ratios of two emission lines, preferably from the same ion, are used to fix the temperature. If the temperature cannot be determined from observations, the emission measure is usually given as the locus of points over a range of temperatures that could produce the observed emission.

Using the upper limits obtained by the DUVE instrument, I can place upper limits to the emission measure of isothermal plasma models for the interstellar medium. We can also consider the effects of absorption on the measurements. In all of these cases I use interstellar abundances as obtained from Spitzer [51].

5.1.1 Limits to local emission measure

In the case of local emission, such as would be expected to be associated with the gas in the local bubble, we would expect minimal dust absorption between us and the emitting gas. In this case, I can use the DUVE emission limits directly to obtain upper limits to the local emission measure.

The emission measure of the interstellar medium is constrained by five emission lines in this band:

1. MgII λ 1027, which peaks at about 1.5×10^4 K, constrains the emission measure at temperatures below 2.0×10^4 K. Because of the nearby interference from Ly β 1025 emission, this limit is very high.

2. CII λ 1037, which peaks at a temperature of about 5×10^4 K, provides the best constraint for temperatures between 2.0×10^4 and 5.1×10^4 K. Because the simple model does not include photoionization, this may understate the constraint, as CII is expected to be produced in large quantities by photoionization due to FUV radiation from stars.

3. CIII λ 977, which peaks at 8.4×10^4 K, provides the best constraint between 5.1×10^4 and 1.0×10^5 K.

4. NIII λ 991, which peaks at 1×10^5 K, constrains the emission measure between 1.0×10^5 and 1.8×10^5 K.

5. OVI $\lambda\lambda$ 1032,1038, which peaks at 2.8×10^5 K, provides the upper limits to emission measure above 1.8×10^5 K.

Figure 5.1 shows these emission measure upper limits. In the figure, the solid line represents limits to local emission measure derived from this work. The dashed lines represent emission measure limits determined by rocket borne broad band X-ray observations in the same direction as the DUVE observations [28]. The dot-dashed line represents limits to emission measure determined by CIV $\lambda\lambda$ 1548,1556 observations by Martin and Bowyer [27]. The dotted line represents upper limits determined by Jelinsky *et al.* [22] from EUVE observations. The hatched area is the parameter space cited by Paresce and Stern as being the allowed region to create observed broadband EUV and soft X-ray emission [30].

5.1.2 Limits to halo emission measure

In the case where the emission is due to non-local gas, such as emission due to a hot galactic halo, we must consider absorption by intervening dust. Using the FUV extinction curve published by Sasseen *et al* [34] and a standard gas to dust ratio, I am able to estimate the optical depth of dust per unit hydrogen column, or equivalent cross section. This equivalent cross section varies nearly linearly between 3.4×10^{-21} cm^2 at 950 Å to 2.6×10^{-21} cm^2 at 1080 Å . Along the lines of sight of the DUVE observations, the mean galactic HI column density is 4.5×10^{20} cm^{-2} resulting in optical depths of between 1.2 and 1.5 and extinctions (1-$e^{-\tau}$) of 72% at 1032 Å . This raises the emission measure limits by a factor of e^{τ}, which is between 3.3 and 4.1 over our wavelength range. These upper limits to halo emission measure are shown in Figure 5.2. As with the previous figure, the dashed lines represent the Wisconsin soft X-ray observations and the dot dashed lines represent the Martin and Bowyer FUV observations. In this case, the dotted line represent emission measure determined from optical observations by Reynolds of the warm ionized phase of the

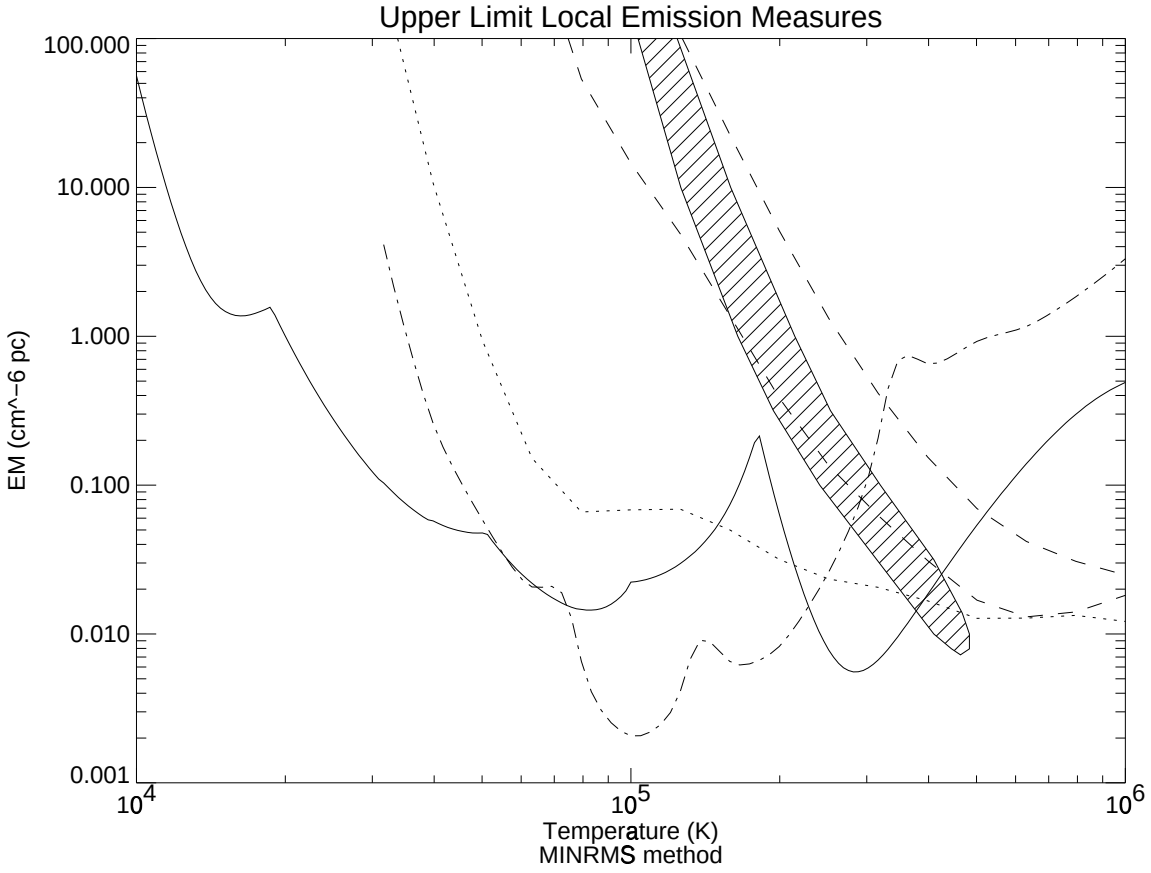

Figure 5.1: Upper limit local emission measures derived from this work are shown as a solid line. The dashed lines represent X-ray emission measure limits derived for Wisconsin B and C band rocket borne observations in this direction. The dot-dashed line represents emission measure limits determined from UVX (1400 to 1800 Å) observations by Martin and Bowyer. The dotted line represents upper limits determined from EUVE observations by Jelinsky *et al.* The hatched area is the parameter space cited by Paresce and Stern as being the allowed region to create observed broadband EUV and Soft X-ray emission.

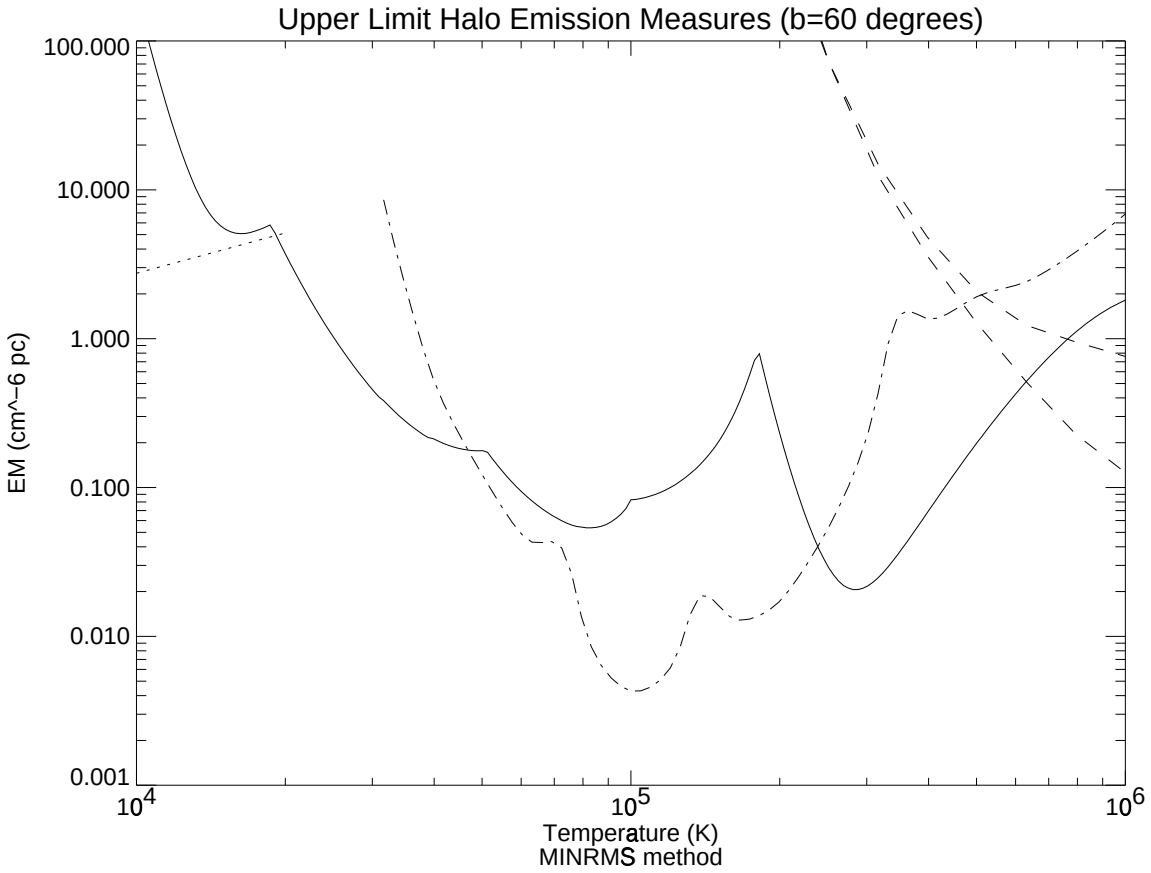

Figure 5.2: Upper limits to the emission measure of the galactic halo as derived by this work are shown as a solid line. The dot-dashed line represents limits to halo emission as determined by Martin and Bowyer from UVX observations. The dashed lines represent B and C band observations by McCammon *et al.* The dotted line represents emission measure limits of the warm ionized ISM as determined from optical observations by Reynolds.

ISM.

5.1.3 Discussion of isothermal models

There is very little that these simple models can reveal about the physics of the interstellar medium. The points where the lines representing various determinations of these limits cross can be used to provide limits to the temperature of the isothermal models. For example in Figures 5.1 and 5.2 we can show that the DUVE observations limit the temperature of an isothermal model of the emission observed by Martin and Bowyer to between 5×10^4 and 2.2×10^5 K. I can also say it limits the temperature of an isothermal model of the gas observed in the soft X-rays to a temperature above 5×10^5 K. Yet this ignores the fact that the gas is undoubtably found in a range of temperatures and the fact that the hot gas will cool over time. Therefore it overlooks any links between the soft X-ray and FUV emitting gas. To explore the evolution of hot gas we must explore more complicated models.

The simplest means of modifying these models is to consider how a distribution of emission measures versus temperature could be obtained. The most obvious means is to calculate how the temperature and density of the gas evolve over time.

5.2 Evolutionary models

In simple evolutionary models of line emission from the hot interstellar medium I consider a steady state, in which there is a source of gas at $T_{\rm hot}$ and a sink of gas at $T_{\rm cold}$ and that the mass flow rates from these sources are equal and constant. In these models we must consider the differential emission measure $\frac{d\rm EM}{dT}$. In general the emergent intensity of a specific line in such a model is going to be:

$$I_{kj} = h\nu_{kj} \int_{T_{\rm cold}}^{T_{\rm hot}} \frac{n_{\rm OVI}}{n_{\rm HI}} \frac{n_{\rm HI}}{n_e} \gamma_{kj}(T) \frac{d(EM)}{dT} dT$$

where EM has its usual definition. This can be simplified by making assumptions about the pressure/density evolution (isobaric or isochoric) and the ionization state of the material involved. Even without such assumptions, the intensity can be calculated numerically by assuming a pressure, density, and temperature distribution.

Because of the importance of nonequilibrium ionization effects in low density gas at the temperature range in question, the assumption of ionization equilibrium may not hold in many cases. Solving for the nonequilibrium ionization state in the absence of photoionization requires solving a system of linear differential equations of the form

$$\frac{dX_i}{dt} = n_e \left[C_{i-1}^{ion} X_{i-1} - (C_i^{ion} + C_i^{rec}) X_i + C_{i+1}^{rec} X_{i+1} \right]$$

where X_i represents the fractional abundance of element X in ionization state i. The C_i^{ion} terms represent all collisional processes leading to ionization from state i to state $i+1$. The C_i^{rec} terms represent all processes leading to recombination from state $i+1$ to state i. These rate coefficients can further be subdivided into

$$C_i^{ion} = C_{elec}^{ion}(i,T) + C_{auto}^{ion}(i,T) + C_{c-t}^{ion}(i,T)$$

$$C_i^{rec} = C_{rad}^{rec}(i,T) + C_{2-e}^{rec}(i,T) + C_{c-t}^{rec}(i,T).$$

C_{elec}^{ion} is the rate coefficient for ionization by collisions with electrons. C_{auto}^{ion} is the rate coefficient for excitation autoionization. C_{rad}^{rec} is the rate coefficient for radiative recombination. C_{2-e}^{rec} is the rate coefficient for dielectronic recombination. The C_{c-t}^{ion} and C_{c-t}^{rec} represent rates for charge transfer ionization and recombination. Because these rates are in general important only for charge transfers from hydrogen and helium atoms to more highly ionized atoms, and because hydrogen and helium are fully ionized in the temperature range of interest, we will ignore these terms. The approximations for these coefficients were taken from Arnaud and Rothenflug, [1] and Shull and Van Steenberg [42].

By assuming a fully ionized plasma of 90% hydrogen and 10% helium as the source of the electron density ($n = 1.91 n_e$), we can solve the set of equations for each element individually. Because the set of equations is stiffly coupled and therefore subject to numerical instability, I integrated them using an implicit multistep stiffly stable method described by Gear [17].

For the purposes of the evolutionary models, a cooling rate was determined from a radiative cooling curve $\Lambda(T)$ and assumed density structure $n(t)$.

$$\frac{dT}{dt} = -\frac{2\Lambda(T)}{3nk} + \frac{2T}{3n}\frac{dn}{dt}$$

$$\frac{dT}{dt} = -\frac{2\Lambda(T)}{3nk} \text{ for isochoric cooling.}$$

$$\frac{dT}{dt} = -\frac{2\Lambda(T)}{5nk} \text{ for isobaric cooling.}$$

The above differential equations thus became

$$\frac{dX_i}{dT} = \frac{\frac{dX_i}{dt}}{\frac{dT}{dt}} = \frac{K n_e^2 k}{\Lambda(T)}\left[C_{i-1}^{ion}X_{i-1} - (C_i^{ion} + C_i^{rec})X_i + C_{i+1}^{rec}X_{i+1}\right]$$

where K=2.87 for isochoric cooling and K=4.78 for isobaric cooling.

The initial conditions for the problem are considered to be the equilibrium ionization values at a temperature of 10^7 K. The quantitly $\Lambda(T)$ was calculated using the emission code of Landini and Monsignori Fossi [26]. New ionization fractions for important elements are calculated numerically using the integration code described above. Emission is then recalculated using the new ionization fractions and summed over all elements to obtain a new $\Lambda(T)$. The procedure is iterated until $\Lambda(T)$ converges.

In this model I assume the dominant cooling mechanism is radiative cooling. Thus the time a parcel of material spends in a given temperature range, and therefore the total amount of material in that range, is inversely proportional to the rate of cooling of such material. Follow the example of Edgar and Chevalier [16, 43], I consider three density/pressure constraints: 1) isobaric evolution wherein all the gas is in pressure equilibrium, 2) isochoric evolution in which all the gas is at a constant density and 3) a mixed model in which the gas is initially evolves isochorically and then at some temperature begins to evolve isobarically. Using the value of the intensity of CIV emission as determined by Martin and Bowyer I can calculate the expected intensity at OVI $\lambda\lambda$ 1032,1038. In the case of an isobaric model, an OVI intensity of 1.9×10^4 ph s^{-1} cm^{-2} str^{-1} is predicted, a factor of 2.5 greater than the upper limit. In the case of an isochoric model, the predicted intensity predicted is 5×10^3 , somewhat below the upper limit. Mixed models fall in between depending on the temperature of the isochoric-isobaric transition. These models will be discussed further in the section of Chapter 6 on galactic fountain models.

These constraints make it unlikely that the CIV emission observed by Martin and Bowyer is due to gas cooling from high temperature ($T > 1\times10^6$ K) at constant pressure.

Chapter 6

Comparison of observations with models of the ISM

6.1 The Smith and Cox model–Scattered Supernova Remnants

The original Smith and Cox model, published in 1974 [46], was based upon a calculation of the volume of the interstellar medium occupied by supernova remnants. They based their model upon earlier calculations of the expansion of isolated supernova remnants with energy 4×10^{50} erg in an ambient medium of density 1.0 cm^{-3}. This calculation resulted in remnants of radius $\sim$ 40 pc which persist for 4×10^{6} years. They calculated a "porosity" of the ISM, $q = r\tau V_{\rm SNR}$ where r is the average supernova rate per unit volume, τ is the lifetime of an isolated SNR, and $V_{\rm SNR}$ is the time averaged volume of the SNR over this lifetime. Their calculation indicated that the value of q was near 0.1. They also estimated that that the probability of intersection of a SNR with others was about 50%, thus understanding these interactions is an important key to the state of the ISM.

The latest revision of the Smith and Cox model has been recently published by Slavin and Cox [44, 45]. In their treatment they describe the spherically symmetric expansion of a supernova remnant into a warm medium of density 0.2 cm^{-3} and

temperature 10^4 K. Their model differs from earlier models in that it includes a magnetic field in the ambient medium which serves to apply an additional nonthermal pressure against the expansion.

Their model involves solving the hydrodynamical equations in spherical coordinates,

$$\frac{d\rho}{dt} = -\frac{\rho}{r^2}\frac{\partial}{\partial r}\left(r^2 v\right)$$

$$\rho\frac{dv}{dt} = -\frac{\partial}{\partial r}\left(P_{th} + \frac{B^2}{8\pi}\right)$$

$$\frac{d}{dt}\left(\frac{P_{th}}{\rho^\gamma}\right) = -\frac{(\gamma-1)}{\rho^\gamma}\left(\frac{1}{r^2}\frac{\partial}{\partial r}\left(r^2 q\right) + L n_e n_H\right)$$

where P_{th} is the thermal pressure, B is the magnetic field strength, γ is the adiabat, L is the radiative cooling coefficient, and q is the radial heat flux.

In their numerical solution to these equations, they assumed that compression and expansion of the matter in the remnant results in a magnetic field that is proportional to the mass density, which is valid for plane parallel shocks. The model assumes an ambient gas density of 0.2 cm^{-3} , a magnetic field in the ambient medium of 5 μG . Because this is a one dimensional model, we would expect these calculations to be valid only along the magnetic equator of a supernova remnant.

The result of their simulation was a bubble of hot gas which reaches its maximum radius of $\sim$ 55 pc after about 1×10^6 years. Following this, the bubble slowly collapses on a time scale of $\sim$ 5.5×10^6 years. Surprisingly, during the collapse, the central temperature stays roughly constant at about 3×10^5 K, while the density inside the remnant increases.

In extending their model from an individual supernova to a model of the interstellar medium, they assumed supernovae distributed randomly throughout the disk with an exponential scale height of 300 pc . They determined the dependence of the maximum radius, expansion time, and collapse time on variations in the magnetic field, gas density, and supernova energy. They used these to determine a global average time integrated volume for a supernova, and used this value to determine a limit volume filling factor of supernova remnants ($q \leq 0.18$). Even with this higher limit

for filling factor, their model shows fewer interactions between remnants than would be expected from the earlier calculation of Smith and Cox [46].

The mean free path between bubbles and OVI column density per bubble in their model closely matches that determined from the analysis of Copernicus observations by Shelton and Cox [41].

6.1.1 Model of FUV emission

For the purposes of applying a Slavin and Cox model to FUV emission measurements it was necessary to simplify the model to some degree.

Rather than duplicate their entire MHD calculation, I was able to digitize several figures from their articles containing density, temperature, velocity, and total pressure profiles of the remnant at various times. I was able to fit these curves with Chebyshev polynomials with time varying coefficients to produce an approximation of the profiles.

Using these density, temperature, pressure, and velocity profiles I was able to calculate the non-equilibrium ionization and the corresponding line emission for a "standard" supernova remnant using the method described in Chapter 4. The average intensity of CIV and OVI emission from this "standard" remnant is shown in Figure 6.1. The diamond represents a value of CIV emission calculated by Slavin and Cox.

I next modeled the appearance of the sky based on the Slavin and Cox model. This required several assumptions in addition to the basic assumptions of the Slavin and Cox model:

- Slavin and Cox assumed a midplane supernova rate of 0.4×10^{-13} pc $^{-3}$ yr^{-1}, and a supernova scale height of 300 pc.

- For the purpose of modeling the distribution of SNRs, Slavin and Cox assumed that all supernovae are "standard" supernovae of energy 5×10^{50} ergs, occurring in a medium of density 0.2 cm^{-3} , temperature of 10000 K, and magnetic field of 5 μG .

- I approximated the effects of limb brightening effects by assuming the ions

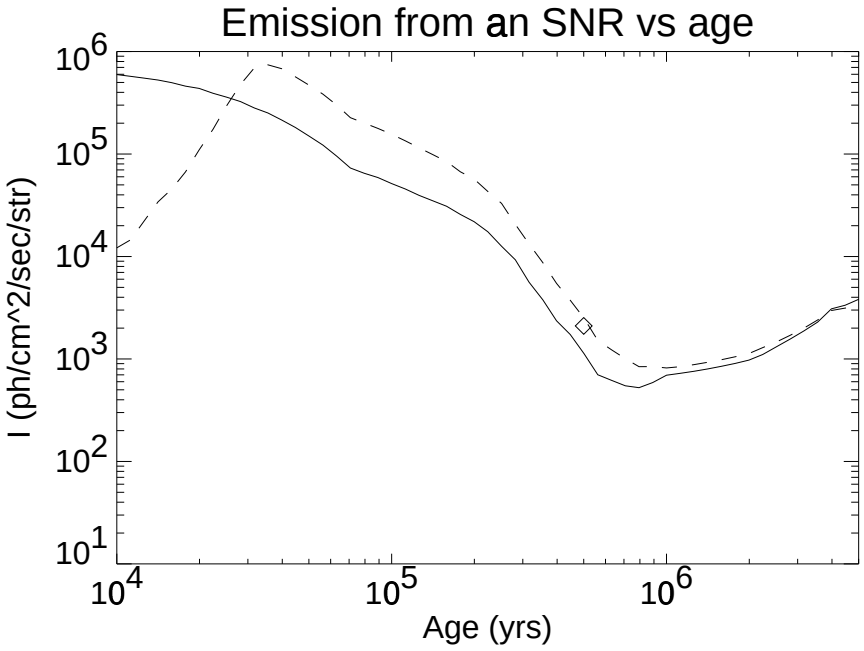

Figure 6.1: A model of OVI (solid line) and CIV (dashed line) emission from a supernova remnant showing variations over time.

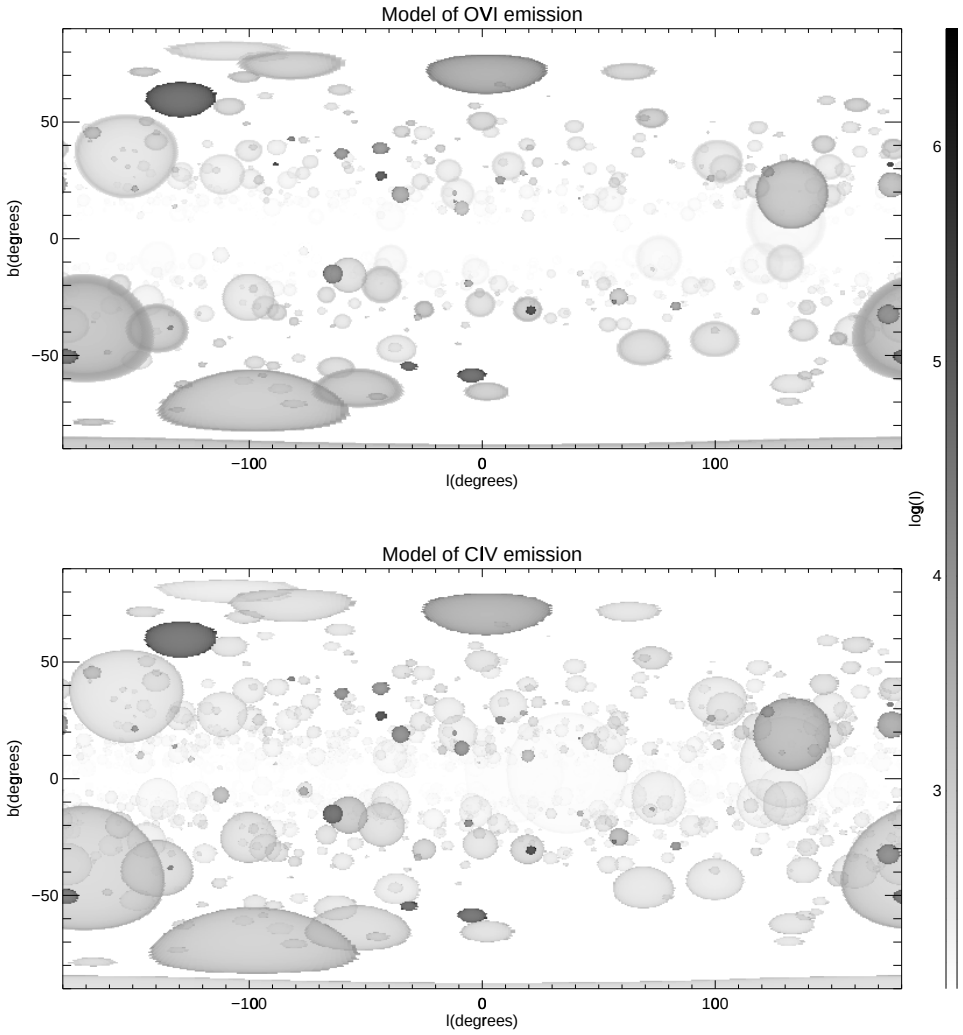

Figure 6.2: CIV and OVI sky maps modeled as scattered supernova remnants. The brightest remnants are $\simeq 1\times10^{6}$ ph s^{-1} cm^{-2} str^{-1}. The faintest distinct remnants are about 200 ph s^{-1} cm^{-2} str^{-1} .

were uniformly distributed within a spherical shell with inner and outer radii determined by the radii where $n_i n_e = \max(n_i n_e)/2$.

- Because Slavin and Cox did not calculate an overall FUV sky brightness, they did not include interstellar opacity in their model. In order to model dust absorption, HI and associated dust were modeled as three components, a Gaussian component of scale length 110 parsecs with central density 0.39 cm^{-3} , a Gaussian component of scale length 260 parsecs and central density 0.11 cm^{-3} , and an exponential component of scale height 400 parsecs and a central density of 0.06 cm^{-3} . H_2 and associated dust were modeled as an exponential distribution with a central density of 1.333 cm^{-3} and with scale height 55 pc [12, 11, 36].

- Interstellar dust opacities at 1032 Å and 1550 Å were determined with reference to Sasseen *et al.* [34, 21] and correspond to cross sections of 2.9×10^{-21} cm^2 N_H^{-1} and 1.5×10^{-21} cm^2 N_H^{-1} respectively.

- The hydrogen column was assumed to be constant across the face of each remnant.

- A small FUV emission component due to the local bubble was modeled as a SNR with central temperature 2×10^6 K, and temperature gradient as specified in Smith and Cox [47].

Maps of CIV and OVI emission in a sample run of this model are shown in Figure 6.2. At both wavelengths the sky brightness is faint, with the median sky intensities being $< I_{OVI} > = 120$ ph s^{-1} cm^{-2} str^{-1} and $< I_{CIV} > = 350$ ph s^{-1} cm^{-2} str^{-1} . As is shown in Figure 6.3, than 5% of the sky emits at the level of CIV seen by Martin and Bowyer, 5000 ph s^{-1} cm^{-2} str^{-1} . In addition to the difference in overall intensity, there is a difference in the distribution of the emission. The CIV intensity measured by Martin and Bowyer is at least a factor of two brighter near the galactic poles than near the galactic plane, whereas in the Slavin and Cox model, the majority of the emission is produced near the galactic plane.

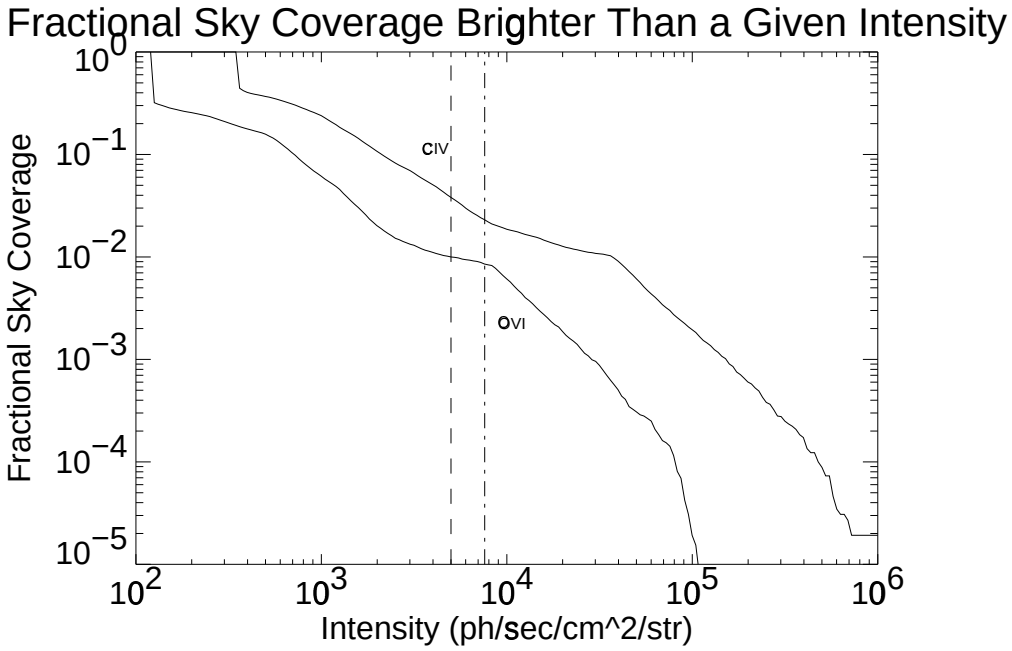

Figure 6.3: Histograms of sky brightness in a Slavin and Cox model. The upper curve represents the fraction of the sky that has CIV emission brighter than the intensity on the horizontal axis. The lower curve shows the same calculation for OVI . The dashed vertical line at 5000 ph s^{-1} cm^{-2} str^{-1} represents the intensity of CIV seen by Martin and Bowyer. The dot-dashed line at 7600 ph s^{-1} cm^{-2} str^{-1} represents the DUVE OVI upper limit.

6.2 The McKee-Ostriker model

In their 1977 paper, McKee and Ostriker presented another calculation of the interstellar porosity. By assuming a lower pressure and density in the ambient medium than that assumed by Smith and Cox, and a higher energy per supernova, they calculated a porosity q which could exceed unity, rendering simple calculations of porosity invalid due to interaction of remnants. Therefore, they assumed that the filling factor of the hot gas was large. Using this, they devised a 3 phase model of the ISM, consisting of warm (10^4 K) spherical clouds, some with cool (10^2 K) cores, existing in pressure equilibrium with a hot ($10^{5.7-6.0}$ K) medium at pressure $10^{3.2}$ K. The model assumed heating of the hot medium by supernovae, and cooling of the hot medium by radiation and by conductive evaporation at the interfaces between the warm clouds and the hot medium.

6.2.1 Constraints to the filling factor of the hot medium

The easiest constraint to place upon a McKee-Ostriker model is that of the filling factor of the hot medium itself. At the parameters specified by McKee and Ostriker, (P=2500 cm^{-3}K , T_{hot}=$10^{5.7}$ to $10^{6.3}$, $f_{hot} = 0.6$), we can calculate the OVI emission measure that would be expected to be present along the DUVE line of sight.

$$\mathrm{EM} = 5.7{\times}10^{-4} \left[\frac{P}{2500\ \mathrm{cm^{-3}K}}\right]^{2} \left[\frac{T_{\mathrm{hot}}}{5{\times}10^{5}K}\right]^{-5.2} \left[\frac{f_{\mathrm{hot}}}{0.6}\right] \left[\frac{h}{1\ \mathrm{kpc}}\right]\ \mathrm{cm^{-6}pc}$$

This is not a very interesting constraint, because even at filling factors of 1, it fails to reach the DUVE OVI upper limits. It shows that detecting the hot medium itself is a difficult task at FUV wavelengths. This is because the bulk of FUV emission in a MO model results from the interfaces between the warm and hot media.

6.2.2 Models of conductive cloud interfaces

To more accurately calculate emission from a MO model, I use an analytic solution for conductive cloud boundaries as described by Dalton and Balbus [10]. This model describes both saturated and unsaturated evaporation of spherical clouds. Saturated

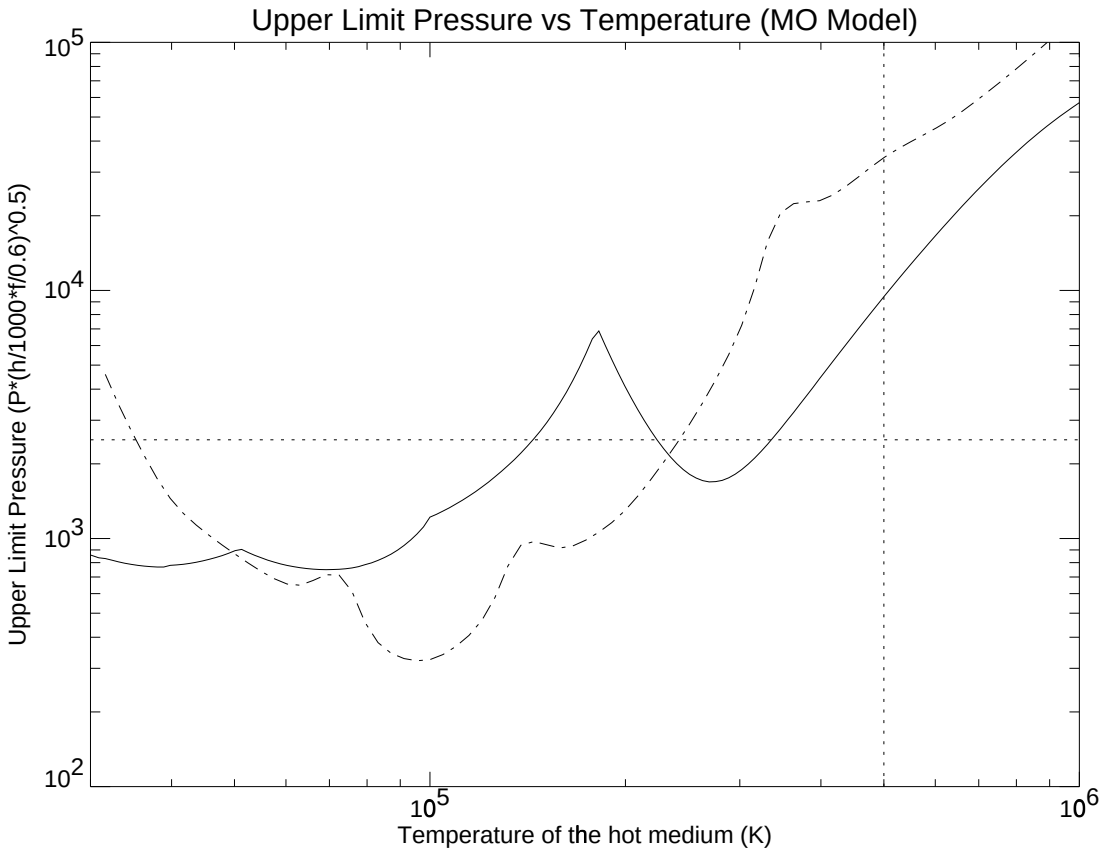

Figure 6.4: Limits to the pressure of the hot medium in a McKee Ostriker model. The solid line represents limits placed by this work. The dashed line represents limits placed by FUV measurements by Martin and Bowyer. The horizontal and vertical lines represent the MO "preferred" values. These limits do not include evaporative cloud boundaries.

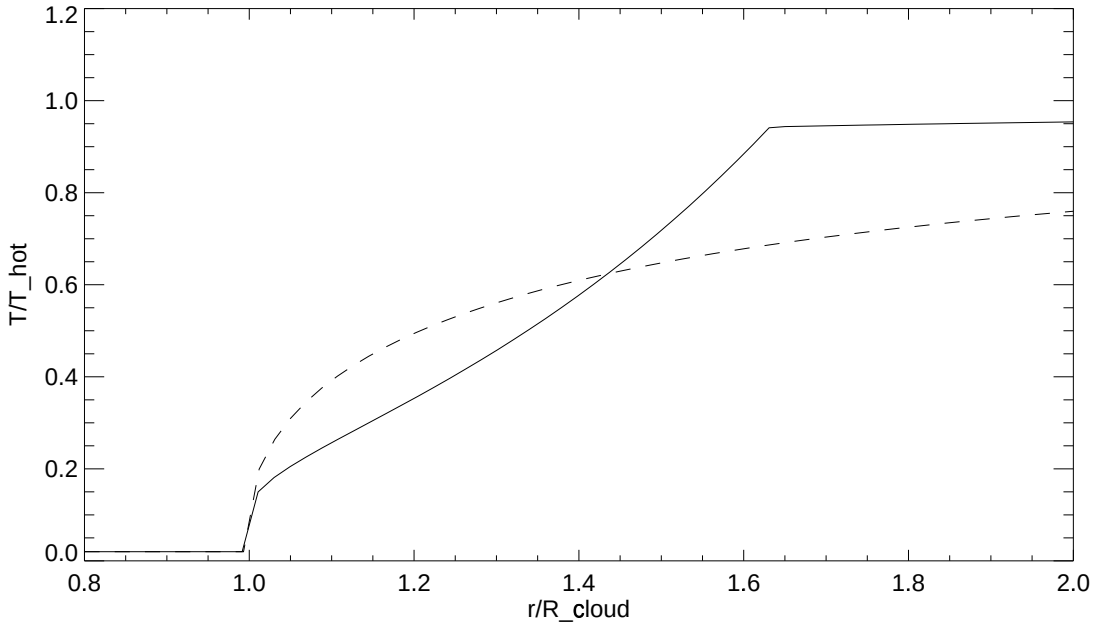

Figure 6.5: Temperature profiles for evaporating clouds with different saturation parameters. ($\sigma = 10$ solid line,$\sigma = 0$ dotted line)

evaporation occurs when the temperature scale heights become large compared to the mean free path of electrons in the gas. This results in a breakdown of the local approach to heat transport; energy is transported many temperature scale heights. The result is that the diffusive approximation ($q = -\kappa \nabla T$) is no longer valid, resulting in much lower heat flux than would be calculated by using the gradient of the temperature. The form of the solutions for density, temperature, and velocity profiles when parameterized to a unitless radius $y = \frac{r}{R_{\rm cloud}}$ and temperature $\tau = \frac{T}{T_{\rm hot}}$ has only one free parameter, the saturation parameter σ_o, which can be approximated as the ratio of the electron mean free path in the hot gas and the cloud radius. Temperature profiles for two saturation parameters are shown in Figure 6.5.

Because the model is at pressure equilibrium, the cloud radius is determined by the mean column density. The model also provides velocities of the evaporating gas, which allow calculation of non-ionization equilibrium effects, as in the previous

chapter. However, because this solution is time independent, the differential equations must be rewritten in the form

$$\frac{dX_i}{dr} = \frac{\frac{dX_i}{dt}}{\frac{dr}{dt}} = \frac{n_e}{v}\left[C_{i-1}^{ion}X_{i-1} - (C_i^{ion} + C_i^{rec})X_i + C_{i+1}^{rec}X_{i+1}\right]$$

In addition, it is assumed that the temperature distribution in this model is determined only by the gas flow and heat conduction, with no radiative losses. This assumption is valid as long as the heating time scale of gas in the flow ($\frac{dT}{dt} = v * \frac{dT}{dr}$) shorter than the cooling time scale for the gas in the flow. Therefore no iteration is required to determine the radiative output of this model.

Because the gas flows outward toward regions of rapidly decreasing density, the ion temperature lags the electron temperature to a substantial degree. As a result the intermediate stage ions can persist much longer than would be expected from collisional ionization equilibrium calculations. This has the result of increasing the ion column densities. In many cases this also results in an increase in the intensity of line emission from these ion. However, for some ions, especially those low stage ions that form very near the cloud boundary where the temperature and density gradients are highest, the intensity of the emission can decrease.

Emission from cloud interfaces

This calculation was repeated for clouds of varying radii and pressures at the "preferred" McKee Ostriker values of the temperature (5×10^5 K) and filling factor (0.6). The resulting emergent intensities from the conductive boundaries were well fit by a power law.

$$I_{\rm OVI}^{cloud} \sim 10.3\left(\frac{P}{2500\ {\rm cm^{-3}K}}\right)^2\left(\frac{N_{\rm HI}^{cloud}}{10^{18}\ {\rm cm^{-2}}}\right)^{1.51}\ {\rm ph\ s^{-1}\ cm^{-2}\ str^{-1}}$$

$$I_{\rm CIV}^{cloud} \sim 34.0\left(\frac{P}{2500\ {\rm cm^{-3}K}}\right)^2\left(\frac{N_{\rm HI}^{cloud}}{10^{18}\ {\rm cm^{-2}}}\right)^{1.65}\ {\rm ph\ s^{-1}\ cm^{-2}\ str^{-1}}$$

Given a power law distribution of clouds with slope (α) and summed column density N_{HI} we can calculate the intensity of emission along a line of sight. I use a power law described by Dickey and Lockman [12] ($\alpha = -4.3$) for clouds with column

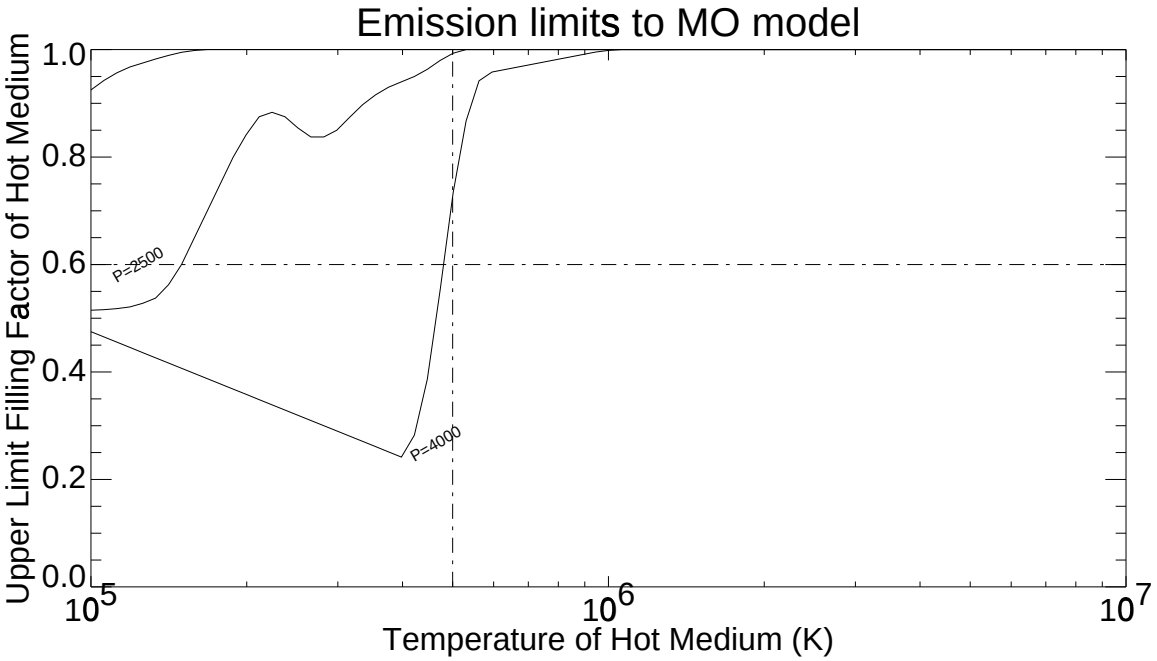

Figure 6.6: The solid lines show the limits to filling factor in an MO model placed by the DUVE data as a function of temperature for 3 assumed pressures. Pressures shown are 320, 2500, and 4000 $\mathrm{cm^{-3}K}$. The horizontal and vertical lines represent the MO preferred values of the temperature and filling factor.

density between 1.5×10^{18} and 1.2×10^{19} and calculate a total emission integrated along the line of sight of

$$I_{\mathrm{OVI}} = 1600 \left(\frac{P}{2500\ \mathrm{cm^{-3}K}}\right)^2 \left(1 - e^{\frac{-N_{18}}{350}}\right)$$

$$I_{\mathrm{CIV}} = 5300 \left(\frac{P}{2500\ \mathrm{cm^{-3}K}}\right)^2 \left(1 - e^{\frac{-N_{18}}{650}}\right)$$

where N_{18} is the total line of sight hydrogen column in units of 10^{18} $\mathrm{cm^{-2}}$.

Along the DUVE line of sight, this would result in emission of 1200 and 2700 ph $\mathrm{s^{-1}\ cm^{-2}\ str^{-1}}$ respectively.

By assuming a pressure, we can determine the locus of values of filling factor and temperature that would produce emission at the DUVE OVI upper limit or CIV emission at the Martin and Bowyer measured level. Such curves are plotted for 3

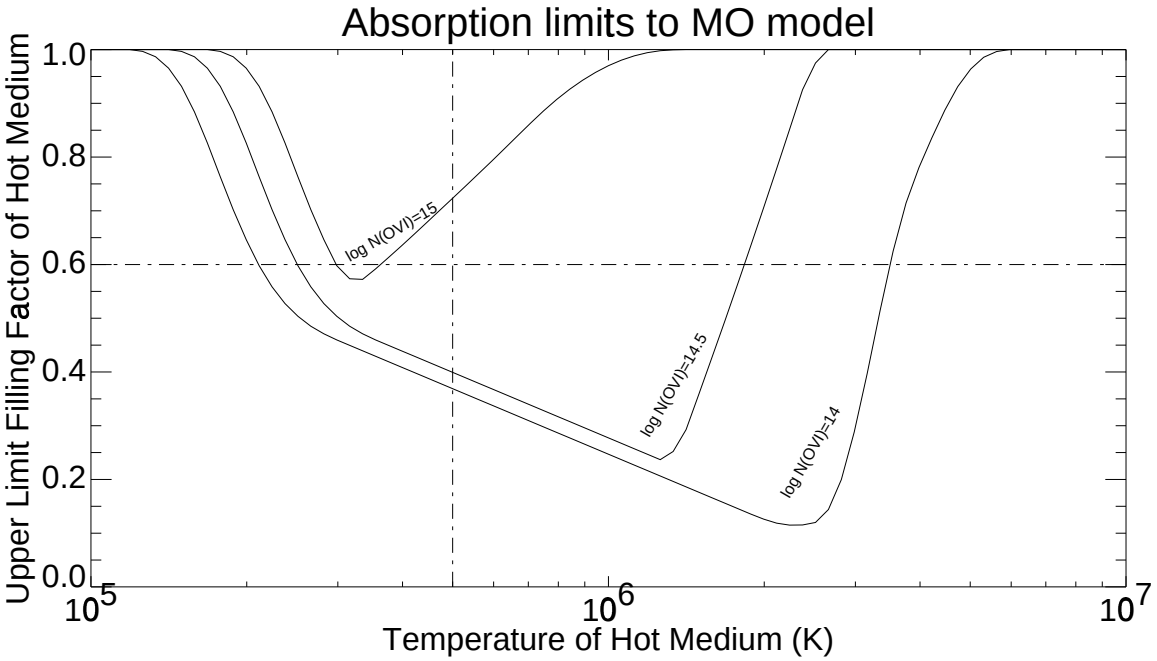

Figure 6.7: Calculations of OVI absorption in a standard MO model. The lines represent contours of constant OVI column densities of 10^{14}, $10^{14.5}$, and 10^{15} cm^{-2} . The highest column densities that have been measured are around $10^{14.5}$ cm^{-2} .

different pressures (320, 2500, and 4000 cm^{-3}K) in Figure 6.6. The area below these curves represent allowed values of the temperature and filling factor.

FUV absorption due to cloud interfaces

It became apparent early in these studies that the McKee Ostriker model over-produced absorption by many of the high ionization species. The thin (compared to a mean free path) envelopes of small clouds allowed high ions to travel very far into the hot medium before being further ionized. And in the case of OVI the "preferred" temperature of the hot medium results in a fairly high OVI fractional abundance (6%).

The effect of these high column densities is shown in Figure 6.7. For the range of temperatures from 10^5 to 10^7 K and for filling factors between 0 and 1, I have

calculated the OVI column density. Contours of constant column density have been plotted on the Figure. For temperatures between 2 and 7×10^5 K, the bulk of the OVI absorption is due to the hot medium itself. At higher temperatures, absorption from the the cloud envelopes begins to become important.

The highest OVI columns that have been measured to date are a few times 10^{14} cm^{-2} [40]. However, the McKee Ostriker preferred values of the temperature and filling factor result in an OVI column of $10^{14.8}$ cm^{-2} , higher than the observed values. The calculations presented here match well with earlier calculations by Dalton and Balbus [10] and Ballet *et al.* [2]. Attempting to understand the discrepancy between these calculated columns and the measured values is the subject of much current research [45, 43, 20]. Many of these studies have concentrated on modeling the microphysics of the boundary layer by adding turbulent mixing of the hot and warm gas.

In the case of a power law distribution, as assumed here, the bulk of both the absorption and the emission are due to interfaces of the smallest clouds. Therefore these results are somewhat sensitive to the slope of the cloud spectrum power law and the lower end size cutoff. In general reducing the slope of the power law results in less absorption, as does increasing the low end cutoff. This may affect the calculated absorption column by up to 20% for power law slopes between -3 and -5.

6.3 Galactic fountain models

Shapiro and Field [38] first described a "galactic fountain" model of the hot interstellar medium. In this model they argued that the long cooling time of hot, low-density gas ($t > 10^6$ yrs) would allow time for the hot gas to rise buoyantly above the galactic plane. This gas would eventually cool radiatively, condense into clouds, and fall back to the plane. They argued that this model could explain both the presence of hot gas and infalling high velocity clouds.

Since this model was introduced, it has been extended by others to include effects such as photoionization, turbulent mixing of hot and warm gas, dissociation of dust, and variations in the temperature of the source gas.

6.3.1 Basic galactic fountain models

Basic galactic fountain models follow the thermal evolution of hot gas. Most of these basic models assume that the gas starts its cooling at a constant density and then, at some point, it transitions to evolution at constant pressure. If we assume the the CIV emission observed by Martin and Bowyer was emission from a galactic fountain, and scale our calculations to this value, we can use these simple models to determine what the expected OVI intensity would be. In these models there are many free parameters, most importantly the temperature of the input gas, and the temperature of the isochoric→isobaric transition. Dust can also be added to the models, resulting in initially rapid cooling due to dissociation of the dust [47].

Calculations for these models were made with the non-equilibrium ionization code described in Chapter 5. We again calculate the time integrated emission for a cooling gas parcel for both isobaric and isochoric cooling. Figure 6.8 shows calculations of OVI emission vs the base temperature for simple isochoric and isobaric galactic fountain models scaled to the Martin and Bowyer CIV emission value (5000 ph s^{-1} cm^{-2} str^{-1}). We have also assumed an intervening hydrogen column of 4.5×10^{20} cm^{-2} when calculating the OVI emission intensity. The dashed line in the lower figure represents the DUVE upper limit. If we assume that the observed CIV emission is produced in a galactic fountain, I can place an upper limit input temperature of 3.5×10^{5} K on fully isobaric fountains. Fully isochoric fountains would produce OVI emission at levels below the DUVE detection threshold.

In Figure 6.9 I show models containing an isochoric/isobaric transition. These models were calculated using the same code, but at a certain temperature, the model transitions from isochoric cooling to isobaric cooling. Again we scale to the Martin and Bowyer CIV value, and assume a hydrogen column of 4.5×10^{20} cm^{-2} . The dashed line in the lower figure represents the DUVE upper limit. In this case I can limit the transition temperatures to less than 2×10^{5} K.

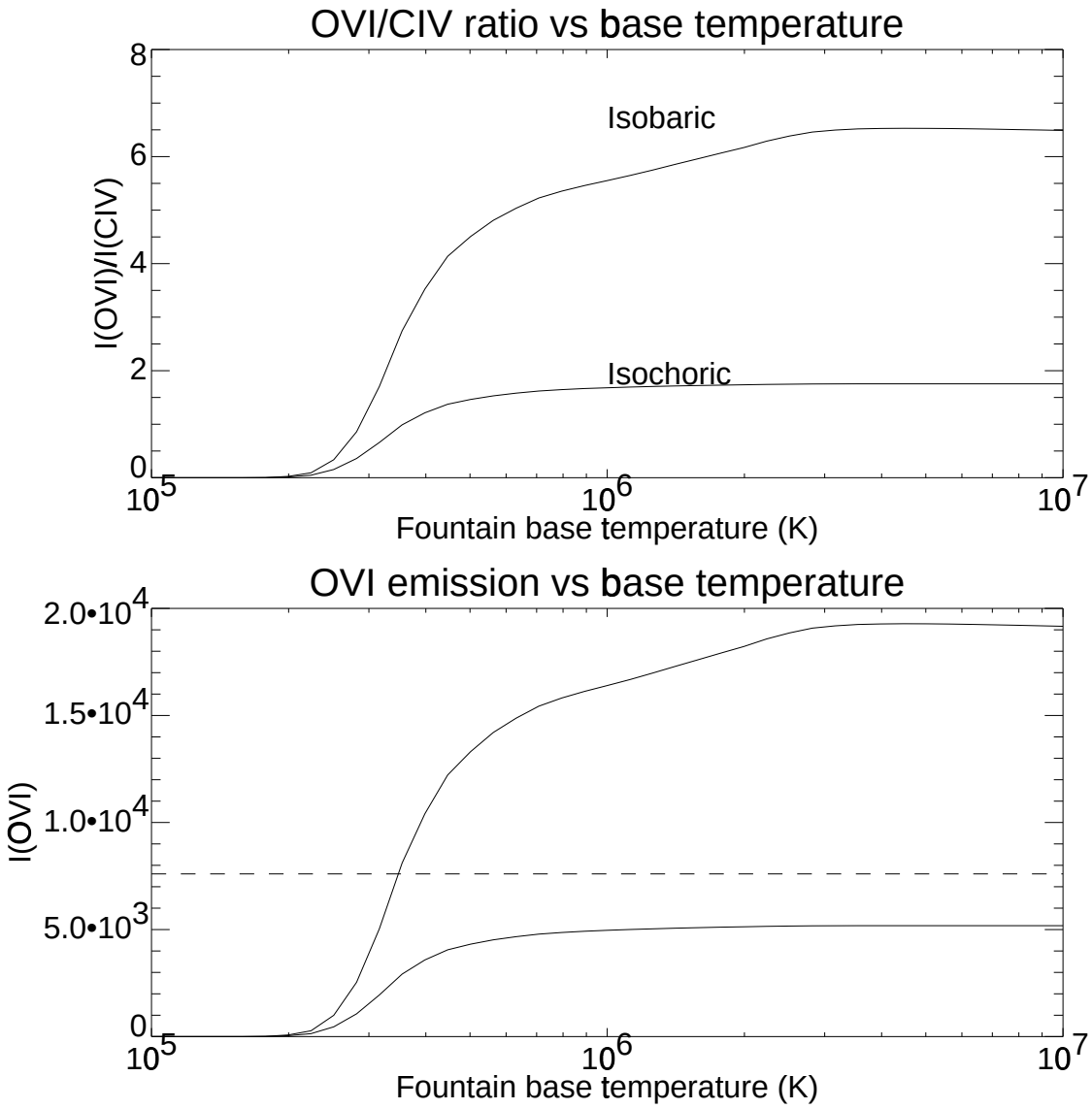

Figure 6.8: OVI emission vs base temperature for simple galactic fountain models. Both isobaric and isochoric models are shown. The lower plot assumes 5000 ph s^{-1} cm^{-2} str^{-1} of measured CIV emission and absorption associated with an HI column of 4.5×10^{20} cm^{-2} . The dotted line represents the DUVE upper limit to OVI emission.

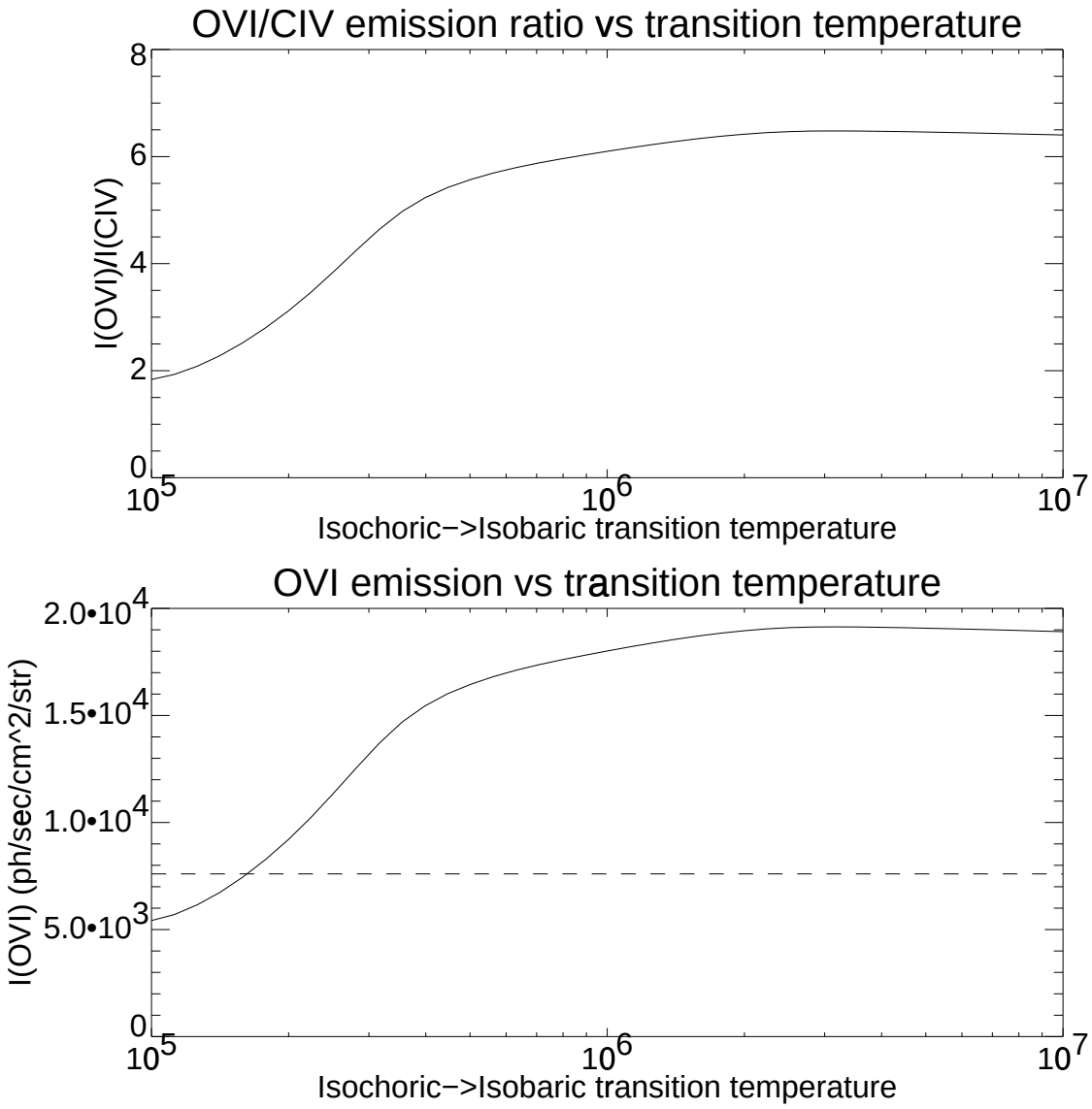

Figure 6.9: OVI emission vs transition temperature for simple galactic fountain models. The lower plot assumes 5000 ph s^{-1} cm^{-2} str^{-1} of CIV emission and absorption associated with an HI column of 4.5×10^{20} cm^{-2} . The dotted line represents the DUVE upper limit to OVI emission.

Model[ref]	Edgar and Chevalier[8, 16]	Houck and Bregman [20]	Shull *et al.* [43]
T_{max} (K)	10^6	3×10^5	$10^{5.3\pm0.3}$
$\frac{I(\mathrm{O\,VI})}{\dot{M}[\odot]}$	1600-2400	1200	200-350
$\frac{I(\mathrm{O\,VI})}{I(\mathrm{C\,IV})}$	7.2–10.8	0.3	1.0–1.4
$\dot{M}_{max}(M_\odot yr^{-1})$	$<$ 3.2–4.75	$<$ 6.3	$<$ 21–38

Table 6.1: Constraints to published galactic fountain models.

6.3.2 Comparisons to other galactic fountain models

Many far more complex models of galactic fountains have been published including effects outside of the realm of the simple models listed above. They have included such things as non-equilibrium ionization, turbulent mixing of hot and cold gas, and photoionization by the emitted EUV and X-ray radiation. However, each model can be reduced to a prediction of the ratio of $\frac{I_{\mathrm{O\,VI}}}{I_{\mathrm{C\,IV}}}$ and the intensity of O VI emission per solar mass of circulation within the fountain. A summary of several of these models is shown in Table 6.1.

The model by Edgar and Chevalier [16] includes non-equilibrium effects at temperatures below 10^6 K, and transitions between isochoric and isobaric evolution. They predict an emission at C IV $\lambda\lambda$ 1549 of 560-890 ph s^{-1} cm^{-2} str^{-1} for a mass flow of 4 $M_\odot$ yr^{-1} and O VI $\lambda\lambda$ 1032,1038 emission of 1600-2400 ph s^{-1} cm^{-2} str^{-1} . I can therefore limit the mass flow rate in their model to less than 4.75 $M_\odot$ yr^{-1}. Their model also predicts $\frac{I_{\mathrm{O\,VI}}}{I_{\mathrm{C\,IV}}} = 7.2 - 10.8$, a much higher value than the observed limit of $\sim$1.5.

The models of Houck and Bregman [20] attempt to fit the observed scale height and velocity distribution of neutral gas clouds in the galaxy with a galactic fountain model. Their models do not include non-equilibrium ionization effects, which they concluded would have little effect on their results Their results were calculated along a one dimensional grid. Their best fit to the distribution of neutral cloud velocities was a model with a base temperature of 3×10^5 K, a base pressure of 300 $cm^{-3}K$, and a mass flow rate of 0.2 $M_\odot$ yr^{-1}. Although Houck and Bregman did not include

explicit predictions of FUV emission, I was able to use data from their paper to produce conservative lower limits to the equilibrium CIV and OVI intensities of this model. By digitizing figures from their paper, I was able to estimate $I_{\rm OVI}$ to be approximately 1200 ph s^{-1} cm^{-2} str^{-1} per solar mass of flow and $\frac{I_{\rm OVI}}{I_{\rm CIV}} = 0.3$. Both of these values are consistent with the DUVE observations as well as those of Martin and Bowyer.

Shull, Slavin and Begelman [45, 43] added the effects of turbulent mixing of hot and cold gas into galactic fountain models. In this model, they calculate that the ratio for emission $\frac{I_{\rm OVI}}{I_{\rm CIV}} = 1.2 \pm 0.2$ for $\log T = 5.3 \pm 0.3$, resulting in a predicted OVI emission of 5000 to 7000 ph s^{-1} cm^{-2} str^{-1} at mass flow rates between 15 and 25 $M_\odot$ yr^{-1}. This ratio is consistent with the DUVE observations. I am able to limit mass flow in this model to 21 to 38 $M_\odot$ yr^{-1}.

Chapter 7

Conclusions

The observations made by the DUVE instrument did not detect any emission from the hot phase of the interstellar medium. I was, however, able to place upper limits to emission from OVI $\lambda\lambda$ 1032,1038 , CII λ 1037 , CIII λ 977, and NIII λ 971 which significantly constrain the parameters of the hot ISM. I have used these limits to determine constraints to the emission measure of both local and halo gas between 10^4 and 10^6 K.

Because the DUVE upper limit is a factor of 4 lower than a measurement reported by Dixon *et al.* I conclude that OVI emission is highly variable over the sky. Because Dixon *et al.* placed upper limits along other lines of sight that were below their measured value, I conclude that it is probably not indicative of emission from the "typical" diffuse ISM.

I have modeled OVI and CIV emission from scattered supernovae. This model produces emission at levels well below the measured CIV values and the DUVE OVI limits. While I cannot rule out this model, I conclude it is unlikely to be responsible for observed emission.

I have modeled OVI and CIV emission from clouds in a standard McKee Ostriker model. The produced emission in this model is also well below the DUVE OVI upper limits and the measured CIV values. However, this model over-produces OVI absorption at the McKee-Ostriker "preferred" parameters. To fit OVI absorption measurements the model would require filling factors $f_{\rm hot} < 0.4$ or temperatures

$T_{\rm hot} > 2{\times}10^6$ K. This discrepancy between the model and observations has been noted in the past, and is being researched in detail by many groups.

I am able to place limits to the base temperatures and isochoric transition temperatures in simple galactic fountain models. My observations seem to be inconsistent with the I[OVI]/I[CIV] ratios predicted by galactic fountain models with base gas temperatures of above about $10^{5.6}$K. My observations are consistent with galactic fountain models with lower temperatures. The observations are able to place limits to the mass flow rates of several models.

Bibliography

[1] Arnaud, M., and Rothenflug, R., A&A Supp., **60**, 425, 1985.

[2] Ballet, J., Arnaud, M., and Rothenflug, R., A&A **161**, 12, 1986.

[3] Blair, W. P., Long, K. S., Vancura, O., and Holberg, J. B., ApJ, **374**, 202, 1991.

[4] Blair, W. P., Vancura, O., and Long, K. S., AJ, **110n1**, 312, 1995.

[5] Bowyer, C. S., Field, G. B., and Mack, J. E., Nature, **351**, 32, 1968.

[6] Chakrabarti, S., Kimble, R. and Bowyer, S., JGR, **89**, 5660, 1984.

[7] Chevalier, R. A., and Fransson, C., ApJ (Letters), **279**, L43, 1984.

[8] Chevalier, R. A., and Oegerle, W. R., ApJ, **227**, 398, 1979.

[9] Cox, D. P., ASP Conf. Series, **80**, 317, 1995.

[10] Dalton, W. W., and Balbus, S. A., ApJ, **404**, 625, 1993.

[11] Dame, T. M., and Thaddeus, P.,ASP Conf. Series, **80**, 15, 1995.

[12] Dickey, J. M., and Lockman, F. J., Ann. Rev. Astr. Ap., **28**, 215, 1990.

[13] Dixon, W. V., Davidsen, A. F. and Ferguson, H. C., ApJ, **465**, 288, 1996.

[14] Edelstein, J. and Bowyer, S., AdSpR, **v13n12**, 307, 1993.

[15] Edelstein, J., Ph. D. Thesis, U. C. Berkeley, 1992.

[16] Edgar, R. J., and Chevalier, R. A., ApJ (Letters), **310**, L27, 1986.

[17] Gear, C. W., *Numerical Initial Value Problems in Ordinary Differential Equations*, Prentice Hall, Inc. (Englewood Cliffs, New Jersey), 1971.

[18] Gladstone, R., Private Communication, 1992.

[19] Holberg, J. B., ApJ, **311**, 969, 1986.

[20] Houck, J. C., and Bregman, J., ApJ, **352**, 506, 1990.

[21] Hurwitz, M., Bowyer S., and Martin, C., ApJ, **372**, 167, 1991.

[22] Jelinsky, P., Vallerga, J. V. and Edelstein, J., ApJ, **442**, 653, 1995.

[23] Jenkins, E. B., ApJ, **219**, 845, 1978.

[24] Jenkins, E. B., ApJ, **220**, 107, 1978

[25] Kruk, J. W., Durrance, S. T., Kriss, G. A., Davidsen, A. F., Blair, W. P., Espy, B. R. and Finley, D. S., ApJ (Letters), **454**, L1, 1995.

[26] Landini, M., and Monsignori Fossi, B. C., A&A (Supplement), **82**, 229, 1990.

[27] Martin, C. and Bowyer, S., ApJ, **350**, 242, 1990.

[28] McCammon, D., Burrows, D. N., Sanders, W. T., Kraushaar, W. L. ApJ, **269**, 107, 1983.

[29] McKee, C. F. and Ostriker, J. P., ApJ, **218**, 148, 1977.

[30] Paresce, F. and Stern, R., ApJ, **247**, 89, 1981.

[31] Raymond, J. C., ApJ, **384**, 502, 1992.

[32] Reynolds, R. J., ApJ (Letters), **372**, L17, 1991.

[33] Sanders, W. T., ASP Conf. Series, **80**, 489, 1995.

[34] Sasseen, T. P., Bull. A.A.S, **188**, 07.02, 1996.

[35] Savage, B. D., and de Boer, K. S., ApJ, **243**, 460., 1981.

[36] Savage, B. D., ASP Conf. Series, **80**, 233, 1995.

[37] Sembach, K. R., Savage, B. D., and Lu, L., ApJ, **439**, 672, 1995.

[38] Shapiro, P. R. and Field, G. B., ApJ, **205**, 762

[39] Shapiro, P. R. and Benjamin, R. A., PASP, **103**, 923, 1991.

[40] Shelton, R. L., Ph. D. thesis, University of Wisconsin, 1995.

[41] Shelton, R. L., and Cox, D. P., ApJ, **434**, 599, 1994.

[42] Shull, J. M., and Van Steenberg, M. ApJ Supp., **48**, 95, 1982.

[43] Shull, J. M., and Slavin, J. D., ApJ, **427**, 784, 1994.

[44] Slavin, J. and Cox, D., ApJ, **392**, 131, 1992.

[45] Slavin, J. and Cox, D., ApJ, **417**, 187, 1993.

[46] Smith, B. W., and Cox , D. P., ApJ (Letters), **189**, L105, 1974.

[47] Smith, R. K., Ph. D. Thesis, University of Wisconsin, 1996.

[48] Snowden, S. L., Freyberg, M. J., Plucinsky, P. P., Schmitt, J. H. M. M., Truemper, J., Voges, W., Edgar, R. J., McCammon, D., and Sanders, W. T, ApJ, **454**, 861, 1995.

[49] Spitzer, L., ApJ, **124**, 20, 1956.

[50] Spitzer, L., ApJ (Letters), **458**, 29, 1996.

[51] Spitzer, L., *Interstellar Processes*, John Wiley & Sons, Inc. (New York), 1978.

[52] Weaver, R., Highlights Astronomy, **3**, 423, 1974.

[53] Wesselius, P. R. and Feyes, I., A&A, **24**, 15, 1973.